

Precise γ -Ray Timing and Radio Observations of 17 Fermi γ -Ray Pulsars

P. S. Ray^{1,2}, M. Kerr³, D. Parent⁴, A. A. Abdo⁵, L. Guillemot⁶, S. M. Ransom⁷, N. Rea⁸,
M. T. Wolff¹, A. Makeev⁴, M. S. E. Roberts⁹, F. Camilo¹⁰, M. Dormody¹¹, P. C. C. Freire⁶,
J. E. Grove¹, C. Gwon¹, A. K. Harding¹², S. Johnston¹³, M. Keith¹³, M. Kramer^{14,6},
P. F. Michelson³, R. W. Romani³, P. M. Saz Parkinson¹¹, D. J. Thompson¹²,
P. Weltevrede¹⁴, K. S. Wood¹, M. Ziegler¹¹,

ABSTRACT

We present precise phase-connected pulse timing solutions for 16 γ -ray-selected pulsars recently discovered using the Large Area Telescope (LAT) on the *Fermi Gamma-ray Space Telescope* plus one very faint radio pulsar (PSR J1124–5916) that is more effectively timed with the LAT. We describe the analysis techniques including a maximum likelihood method for determining pulse times of arrival from unbinned photon data. A major result of this work is improved position determinations, which are crucial for multi-wavelength follow up. For most of the pulsars, we overlay the timing localizations on X-ray images from *Swift* and describe the status of X-ray counterpart associations. We report glitches measured in PSRs J0007+7303, J1124–5916, and J1813–1246. We analyze a new 20 ks *Chandra* ACIS observation of PSR J0633+0632 that reveals an arcminute-scale X-ray nebula extending to the south of the pulsar. We were also able to precisely localize the X-ray point source counterpart to the pulsar and find a spectrum that can be described by an absorbed blackbody or neutron star atmosphere with a hard powerlaw component. Another *Chandra* ACIS image of PSR J1732–3131 reveals a faint X-ray point source at a location consistent with the timing position of the pulsar. Finally, we present a compilation of new and archival searches for radio pulsations from each of the γ -ray-selected pulsars as well as a new Parkes radio observation of PSR J1124–5916 to establish the γ -ray to radio phase offset.

Subject headings: Gamma rays: stars, pulsars: general, Radio continuum: stars, X-rays: stars

¹Space Science Division, Naval Research Laboratory, Washington, DC 20375, USA

²email: Paul.Ray@nrl.navy.mil

³W. W. Hansen Experimental Physics Laboratory, Kavli Institute for Particle Astrophysics and Cosmology, Department of Physics and SLAC National Accelerator Laboratory, Stanford University, Stanford, CA 94305, USA

⁴Center of Earth Observation and Space Research, College of Science, George Mason University, Fairfax, VA 22030, resident at Naval Research Laboratory, Washington, DC 20375

⁵National Research Council Research Associate, National Academy of Sciences, Washington, DC 20001, resident at Naval Research Laboratory, Washington, DC 20375

⁶Max-Planck-Institut für Radioastronomie, Auf dem Hügel 69, 53121 Bonn, Germany

⁷National Radio Astronomy Observatory (NRAO),

Charlottesville, VA 22903, USA

⁸Institut de Ciències de l'Espai (IEEC-CSIC), Campus UAB, 08193 Barcelona, Spain

⁹Eureka Scientific, Oakland, CA 94602, USA

¹⁰Columbia Astrophysics Laboratory, Columbia University, New York, NY 10027, USA

¹¹Santa Cruz Institute for Particle Physics, Department of Physics and Department of Astronomy and Astrophysics, University of California at Santa Cruz, Santa Cruz, CA 95064, USA

¹²NASA Goddard Space Flight Center, Greenbelt, MD 20771, USA

¹³CSIRO Astronomy and Space Science, Australia Telescope National Facility, Epping NSW 1710, Australia

¹⁴Jodrell Bank Centre for Astrophysics, School of Physics and Astronomy, The University of Manchester, M13 9PL, UK

1. Introduction

Pulsar timing involves making precise measurements of pulse times of arrival (TOAs) at an observatory (or spacecraft) and then fitting the parameters of a ‘timing model’ to those measurements. This powerful technique enables extremely high precision measurements that probe numerous topics in fundamental physics and astrophysics. This is due to the ability to construct a coherent timing model that accounts for every rotation of the neutron star over periods of years. Precise timing measurements on radio pulsars have yielded many fundamental advances including the first indirect detection of energy loss due to gravitational radiation (Taylor et al. 1979) and confirmation of many effects predicted by General Relativity (Stairs 2003; Kramer & Wex 2009).

Until recently, pulsar timing was only practical in the radio and, in some cases, soft X-ray bands (Jackson & Halpern 2005; Livingstone et al. 2009, for example). For radio and X-ray quiet/faint pulsars discovered with the Large Area Telescope (LAT) on *Fermi*, the only option is to time them directly using the γ -ray data. Earlier instruments, such as EGRET on the *Compton Gamma-Ray Observatory*, required very long exposures to even detect a handful of γ -ray pulsars and it only observed them occasionally, typically during a few 2-week viewing periods spread over the 9-year mission. With the LAT, we have a vastly more powerful instrument for long-term pulsar studies. First, its effective area ($\sim 8000 \text{ cm}^2$ at 1 GeV), energy coverage (20 MeV to $> 300 \text{ GeV}$) and point spread function ($\sim 0.8^\circ$ at 1 GeV) are greatly improved, providing a large increase in instantaneous sensitivity over EGRET (Atwood et al. 2009). Second, because *Fermi* operates in a continuous all-sky survey mode with a very large field of view ($\sim 2.4 \text{ sr}$), it accumulates data on all pulsars in the sky roughly uniformly at all times. This allows long evenly-sampled timing observations of all pulsars detectable with *Fermi*.

In this paper, we describe the techniques developed for precise timing of pulsars using the γ -ray photon data provided by the LAT. We then apply this method to the first 16 γ -ray-selected pulsars discovered in blind searches of LAT data (Abdo et al. 2009a) plus one additional radio pulsar (PSR J1124–5916), which is too faint for routine radio

timing (Camilo et al. 2002). The timing models presented here are updated versions of those used for these pulsars in the First LAT Catalog of Gamma-ray Pulsars (Abdo et al. 2010d), and this paper documents the methods used to create those models. In the case of the bright Vela and Geminga pulsars, these methods were used to provide high-precision timing models used for phase-resolved analysis (Abdo et al. 2010e,b).

Timing observations provide a wealth of important information critical to the understanding of these newly-identified pulsars. First, one gets a measurement of the period and period derivative of the source. Having these two numbers allows us to derive estimates of several key parameters including the characteristic age, the inferred dipole magnetic field strength, and the spindown energy loss rate. These parameters are fundamental to understanding the astrophysics of the system. For example, the characteristic age is useful (though certainly not definitive) in the context of arguments for or against associations with supernovae and pulsar wind nebulae (PWNe).

The next critical parameter in the timing model is the pulsar position. Estimating the source position from the reconstructed photon arrival directions can yield localizations that are good to a few arcmin, but to do better than this requires timing. For young or middle-aged pulsars, the LAT can measure pulse arrival times with accuracies of order a millisecond¹, which can be fit to determine positions to arcsecond accuracy. Accurate positions then allow deep counterpart searches in the X-ray, optical, and radio bands, and remove the effects of position error on the remaining timing parameters, most notably the spin-down rate.

Once the basic spin and position parameters are well determined, timing allows us to investigate the rotational irregularities that are common in young pulsars. The primary phenomena are timing noise and glitches. Glitches are sudden increases in pulse frequency with a magnitude in the range $\Delta\nu/\nu \sim 10^{-10} - 10^{-5}$, which provide valuable information about the superfluid interior of neutron stars (Andersson et al. 2003; Link

¹The accuracy of a pulse time of arrival measurement is determined by the photon statistics and the sharpness of the features in the pulse profile. It is always considerably larger than the $\sim 1 \mu\text{s}$ accuracy on individual photon event times recorded by the LAT.

et al. 1999, for example). Timing noise is unmodeled low-frequency (often quasi-periodic) noise observed in the residuals of many pulsars after all the deterministic spin-down effects have been removed. The magnitude of the timing noise has been shown to correlate with frequency derivative (i.e. torque) (Cordes & Downs 1985; Arzoumanian et al. 1994a; Hobbs et al. 2010), but its nature remains poorly understood.

Using the timing positions for these pulsars, we have also undertaken deep radio observations of the γ -ray-selected pulsars to search for radio pulsations. These searches have resulted in three discoveries of radio pulsations, which have been published elsewhere (Camilo et al. 2009; Abdo et al. 2010c). Here, we compile the upper limits from our observations, and from the literature, for the remaining pulsars. These are important inputs to population statistics and modeling of these apparently radio quiet pulsars (Yadigaroglu & Romani 1995; Story et al. 2007, for example), as well as for guiding future deeper searches.

2. Methods

2.1. Data Selection

For the current analysis we use LAT data from 2008 August 4 through at least 2010 February 4, the first 18 months of LAT survey operations. We select LAT events from the most restrictive “dif-fuse” class of the “Pass 6” event reconstructions (Atwood et al. 2009) with a zenith angle of $< 105^\circ$ to reduce contamination from atmospheric secondary γ rays from near the Earth’s limb. For each pulsar, we find an optimal radius and low energy cut to maximize the pulse detection significance. The radius cuts ranged from 0.5 – 1.6° , while the low energy cuts ranged from 50 – 900 MeV. Only photons that pass these cuts are included in the timing analysis.

The number of photons surviving these cuts ranged from 1,174 (PSR J0633+0632) to 14,875 (PSR J1836+5925) in our 18 months of observing, a span in which the pulsars completed several hundred million rotations. This emphasizes the unique nature of timing pulsars using extremely sparse γ -ray data. Typically only of order 100 photons go into each TOA determination. In addition, unlike with radio pulsar timing, the integration time per TOA is equal to the spacing between

TOAs, requiring the model to maintain phase accuracy over a much longer time than is required for radio pulsar timing where the integration time for a TOA is only minutes or hours. We constructed initial models using the `prepfold` tool from the PRESTO pulsar analysis software package². This tool performs epoch folding searches over narrow ranges of frequency and frequency first and second derivatives around the ν and $\dot{\nu}$ values found from the blind search to maximize the signal-to-noise ratio. Combined with searching over a grid of possible pulsar positions, we are able to arrive at an initial model that maintains coherence well enough for TOAs to be determined and the pulsar timing to proceed as described below.

2.2. Geocentering

Pulsar timing software generally expects pulse TOAs to be measured at an observatory that is at a fixed geographic location on the Earth. Observations from a spacecraft in orbit about the Earth obviously do not satisfy this condition and this must be accounted for before computing a pulse arrival time. One could go directly to a time scale (such as TDB) at the solar system barycenter, but this requires a precise knowledge of the pulsar location before the correction can be done and removes the possibility of fitting for the pulsar position as part of the timing model. Instead, in order to remove the effects of the spacecraft motion on the photon arrival times while maintaining the ability to fit for astrometric parameters in the timing model, we correct the measured times to a fictitious observatory located at the Earth’s geocenter.

LAT photon times are recorded in Mission Elapsed Time (MET), which is referenced to Terrestrial Time (TT) via the MJDREF keyword in the FITS file header³. Time is maintained on-board the spacecraft to an accuracy of better than $1 \mu\text{s}$ using a GPS receiver (Smith et al. 2008).

The geocentric time is the satellite time corrected for geometric light travel time to the geocenter. It does not include relativistic terms in

²Available from <http://www.cv.nrao.edu/~sransom/presto/>

³See OGIP Memo OGIP/93-003 http://heasarc.gsfc.nasa.gov/docs/heasarc/ofwg/docs/rates/ogip_93_003/ogip_93_003.html

the correction. The geocentric photon time t_{geo} is defined as

$$t_{\text{geo}} = t_{\text{obs}} + \frac{\mathbf{r}_{\text{sat}}}{c} \cdot \hat{\mathbf{n}}_{\text{psr}}, \quad (1)$$

where \mathbf{r}_{sat} is the vector pointing from the geocenter to the spacecraft, $\hat{\mathbf{n}}_{\text{psr}}$ is a unit vector pointing in the direction of the pulsar (here assumed to be at an infinite distance), and c is the speed of light.

This correction is applied using the *Fermi* science tool⁴ `gtbary` with the `tcorrect=geo` option. After this correction, the time system for the events is still TT, but all times are referenced to the geocenter. This correction has a maximum amplitude of 23.2 ms. Therefore, an error in the assumed pulsar direction as large as 1° causes a maximum error in the corrected time of only 0.4 ms.

2.3. TOA Determination

A TOA is determined from the photon times in a segment of data by first assigning pulse phases to each photon based on an initial model, then measuring the phase offset (Δ) required to align a standard template profile with the measured pulse profile (see Figure 1). This offset is then converted to a time using the pulse period (P) and added to the observation start time, T_0 , to become the measured TOA.

$$\text{TOA} = T_0 + \Delta \times P \quad (2)$$

This TOA is the time when the fiducial point on the pulse profile arrived at the observatory, for a representative pulse during the observation interval. In the case of the geocentered LAT events the TOA is for a fictitious observatory at the geocenter (observatory code `coe` in TEMPO2; Hobbs et al. (2006)). The measurement can be made using binned pulse profiles (as in Figure 1) or directly from the unbinned photon phases, as described below.

For this work, we divide the full 18-month observation interval into segments of equal duration and determine a pulse time of arrival from each segment. The length of each segment is a balance between signal-to-noise ratio and time resolution. Longer integrations result in better signal-to-noise

ratio and smaller statistical measurement errors on each TOA. On the other hand, shorter integrations provide finer time resolution that better samples the annual sinusoidal signal caused by the Earth’s motion around the Sun and the timing noise in some very noisy young pulsars. Therefore we try to achieve at least 1 TOA per month. Fainter pulsars that require a substantial fraction of a year, or longer, per TOA measurement will be difficult to time with the LAT.

For most radio pulsar timing, the TOAs are determined from binned data. The start time of the observation is precisely known from the observatory clock. During the observation, data are folded using *predicted* phases for the pulsar based on a provisional ephemeris (e.g. using the `-polyco` option to TEMPO2), and a binned profile for that observation is computed. The arrival time is computed by cross-correlating the observed profile with a high signal-to-noise template profile with the same binning. The accuracy of this measurement is improved if the cross-correlation is implemented as a fit to a linear phase gradient in the Fourier domain (an application of the Fourier shift theorem), rather than as a simple time-domain cross correlation (Taylor 1992). Finally the TOA is determined as the observation start time plus the measured phase offset (converted back into time units).

The binned TOA determination method can also be applied to photon data, such as that from the LAT, by computing the predicted phase for each photon and building a binned pulse profile from the events. However, since we must make TOA measurements based on a small number of detected photons (often < 100 photons go into each TOA), we can improve the TOA determinations by using an unbinned likelihood analysis to compute the TOA directly from the set of photon phases. This has been discussed before (Livingstone et al. 2009), but we have developed and generalized the technique and describe it in detail here.

We use an unbinned maximum likelihood method to estimate both the light curve template and the TOAs with associated errors. In the likelihood formulation, the template is interpreted as a periodic probability density function to observe a photon at a given phase, $f(\phi; \lambda, \Delta)$, with λ some set of parameters describing the light

⁴<http://fermi.gsfc.nasa.gov/ssc/data/analysis/documentation/>

curve morphology and Δ accounting for the phase shift between the template and the given data set. The TOA is determined by Δ . The template is normalized such that $\int d\phi f(\phi; \lambda, \Delta) = 1$.

We first start with a description of the template, $f(\phi; \lambda, \Delta)$, which must be a continuous function that can be evaluated at any value of ϕ . In many cases, the statistics are sufficiently limited that the pulse profile can be described as a sum of a constant background component and a small number of gaussian peaks. That is,

$$f(\phi) = (1 - \sum_{i=1}^{N_p} p_i) + \sum_{i=1}^{N_p} p_i g(\phi, x_i, \sigma_i), \quad (3)$$

with N_p the number of gaussian peaks, p_i the fraction of the total emission belonging to each peak, and $g(x, \sigma)$ a gaussian with mean x and standard deviation σ . The domain of the gaussian functions is assumed to be wrapped to $[0, 1)$. Here, Δ can be associated with x_1 , the location of the first peak, while the remaining parameters are subsumed in λ .

With increasing statistics, the complexity of GeV light curves is no longer well-represented by a simple sum of components. Bridge emission and peak asymmetry appears, and in general, no simple functional form is sufficient to describe the profile (e.g. the Vela pulsar (Abdo et al. 2010e)). In this case, we prefer kernel density estimation (KDE) methods (de Jager et al. 1986). These methods result in a faithful, non-parametric representation of the light curve. However, even for bright pulsars, the available statistics are such that KDE methods produce a template with broadened peaks and “noisy” valleys, neither of which is desirable for the calculation of a TOA. A good estimator for the template should provide a smooth template (ignore fluctuations) while simultaneously preserving the structure and sharpness of the peaks, which is important because the template sharpness is a factor in the accuracy of the TOA measurements. We outline two approaches we have found effective below.

The first forms the basis for the H-test statistic often used to assess pulsation significance in the absence of a template (de Jager et al. 1989). Coefficients of a Fourier expansion are estimated directly from the unbinned phases. For n photons,

the coefficients for the k th harmonic are

$$\alpha_k = \frac{1}{n} \sum_{i=1}^n \cos(k\phi_i), \beta_k = \frac{1}{n} \sum_{i=1}^n \sin(k\phi_i) \quad (4)$$

and the light curve is given by

$$f(\phi) = 1 + 2 \sum_{k=1}^m \alpha_k \cos(k\phi) + \beta_k \sin(k\phi). \quad (5)$$

The only free parameter is the overall phase of the light curve; variation can be implemented with the Fourier shift theorem or simply by adding a constant phase to the data. The number of harmonics retained should offer an optimum balance between peak “sharpness” and noise in the remainder of the profile. We call this the ‘empirical Fourier’ (EF) method.

The second method is a gaussian KDE *with a phase-dependent bandwidth*, the idea being to use smaller bandwidth for the peaks while smoothing the valleys with a broader kernel. Here, $f(\phi) = \sum_{i=1}^n g(\phi, \phi_i, \sigma_i)$, with g again the standard gaussian. The bandwidth is determined by $\sigma_i = (f_{\max} - f_{\min})/f(\phi_i)\sqrt{n}$. Lest the reader worry about this circular definition, in practice we begin with a phase-independent bandwidth $\sigma = \sqrt{n}$ and iterate. As with the Fourier expansion, the only free parameter is the overall template offset.

In summary, for our template, we choose one of the three above methods (Gaussian, EF, KDE) that produces the best results, as evidenced by the smallest RMS residuals. A comparison of a pulse profile fitted with the three different templates is shown in Figure 2. The template choice is documented for each pulsar.

With the template defined, the next step is to fit for the TOA from each segment of data, always using the chosen template to define the pulse profile and fiducial point. For the fitting, we start with an approximate timing solution (say from a ν - $\dot{\nu}$ search) and fold the photon arrival times to obtain a set of phases $\{\phi_1, \phi_2, \dots, \phi_n\}$. The probability to observe these data, given the light curve model, is formally inverted to form the log likelihood for the parameters, $\sum_{i=1}^n \log f(\lambda, \Delta; \phi_i)$. The parameters are varied to maximize the log likelihood. In the case of a multi-gaussian template, the full dataset is used to determine λ , while in determining TOAs, only Δ is fit. The likelihood surface

generally has a gaussian shape near the best-fit value for Δ , and we estimate the error on Δ by measuring and inverting the curvature of the log likelihood function at the best-fit value. Thus, to determine a TOA, the above fit is carried out for each subset to estimate for Δ and its error σ_Δ .

We mention here an additional challenge brought on by morphology of GeV light curves. An appreciable fraction of pulsars observed so far present light curves with two peaks of similar height with a separation close to 0.5 periods. These light curves are approximately invariant under a half-period translation, and statistical fluctuations may then lead to a likelihood maximum associated with the “wrong” peak. When this happens, a blind search for the maximum likelihood will result in a TOA off by $0.5/\nu$ seconds which must be excluded from the timing solution fit. To avoid loss of data, rather than employing a blind search, we “track” the solution. That is, provided the trial solution is sufficiently good (and this is always the case with iteration), the drift of the actual arrival time from the predicted arrival time is much less than half of a period. We then simply restrict the search for the likelihood maximum to within a range that excludes the “wrong” peak.

2.4. Fitting Timing Models

The measured sets of TOAs are then fitted to a timing model using the pulsar timing software TEMPO2 (Hobbs et al. 2006; Edwards et al. 2006). There are many parameters that can be used in the timing models. For all pulsars we fit for pulse frequency (ν) and frequency first derivative ($\dot{\nu}$) and frequency second derivative ($\ddot{\nu}$). We fit for $\ddot{\nu}$ as a measure of the timing noise present in each pulsar. In most cases, a significant $\ddot{\nu}$ is not detected and we report a 2σ upper limit on the magnitude $|\ddot{\nu}|$. In the cases where $\ddot{\nu}$ is measured, we attribute this solely to timing noise as the $\ddot{\nu}$ expected from any reasonable braking index would be immeasurable over our 18 month data span. If this is still insufficient to whiten the residuals, we add a third frequency derivative, or harmonically related sinusoids (WAVE parameters in TEMPO2, see Hobbs et al. (2004)) to the fit until a satisfactory model is achieved. Note that because of large covariances between the parameters, one should avoid fitting the position and WAVE parameters at the same time.

Finally, in three cases (PSRs J0007+7303, J1124–5916, J1813–2332), a glitch was observed and several glitch parameters were added to the fit, as described in §3.

In our models, the absolute phase 0.0 is arbitrary. In the case of pulsars with both radio and γ -ray emission the convention is usually to assign phase 0 as the peak of the radio pulse (as a proxy for the more physically meaningful point of closest approach of the magnetic axis to the line of sight). However, since we don’t observe radio pulsations from most of these pulsars we have not attempted to define a particular phase 0. However, we do report the parameter TZRMJD for our models, which is the reference for phase 0.0. Phase 0.0 is the pulse phase at the time TZRMJD at the geo-center at infinite frequency.

As a final note, we want to emphasize that different timing models are appropriate for different purposes. One of the primary goals of this work is to use the capability of pulsar timing with the LAT to make accurate localizations of γ -ray-selected pulsars, thus enabling multiwavelength studies of potential counterparts. A secondary goal is characterizing the timing noise in this set of pulsars. For other purposes, different models are appropriate. In particular, for many studies it would be preferable to freeze the position using an accurately known counterpart position (from *Chandra* X-ray observations, for example) to reduce the number of free parameters in the model.

The TEMPO2 timing models described here will all be made available electronically at the Fermi Science Support Center (FSSC) web site⁵.

2.5. A Tempo2 Plugin For Assigning Photon Pulse Phases

One important use of the timing models presented here is to be able to assign an accurate pulse phase to each photon in a LAT observation of a particular pulsar. This is needed for studies of the γ -ray light curve, phase-resolved spectroscopy, or “gating” the data on the off-pulse region to blank out a pulsar to enable studies of faint sources nearby (e.g. Cyg X-3 (Abdo et al. 2009c)). The standard *Fermi* Science Tool `gtpphase` tool was developed for this application. However it

⁵<http://fermi.gsfc.nasa.gov/ssc/data/access/lat/ephems/>

suffers from the limitation that it cannot represent the full complexity of pulsar timing models that include frequency derivatives above $\ddot{\nu}$, glitches, parallax, proper motion, or WAVE parameters. TEMPO2, on the other hand, allows all of these as well as several additional orbital models for pulsars in binary systems.

For these reasons, we have implemented a graphical plugin for calculating pulsar phases for *Fermi*-LAT data with TEMPO2, called `fermi_plugin.C`. This plugin takes LAT event (“FT1”) files with the photon arrival dates, spacecraft (“FT2”) files with the satellite position as a function of time, and TEMPO2 timing solutions and writes photon pulse phases in the FT1 event file. It uses the same spacecraft position interpolation algorithm as implemented in the *Fermi* science tool `gtbary`⁶ and derives barycentric photon times with analogous methods. The barycentric times are then treated as TOAs to find the pulsar phases relative to the absolute phase reference given by the TZR-MJD parameter in the input ephemeris. The plugin thus allows *Fermi*-LAT data analysis with an ephemeris built from radio, X-ray or γ -ray TOAs, with virtually unlimited complexity in the timing model. The plugin has been shown to reproduce the results from the Science Tools when working in `tempo1` emulation mode, but using this mode is not required. It is available in the TEMPO2 sourceforge distribution⁷ and from the Fermi Science Support Center⁸. This plugin is suitable for use with any of the timing models presented here.

3. Results

In this section, we present details of the timing models for each of the 17 pulsars listed in Table 1. The models are determined from the data set as described above. The statistical errors on the parameters are the (single parameter $1\text{-}\sigma$) uncertainties reported by TEMPO2 from the fits. For the pulsars with no $\ddot{\nu}$ required in the model, we estimate the statistical error in the position fit from a fit with $\ddot{\nu}$ free, because this results in a more conservative error estimate that better accounts for the correlations between the astrometric and spin

parameters.

The errors on the position in the tables and shown in the figures are statistical only (though in the figures they are 95% confidence, rather than $1\text{-}\sigma$ since that is the standard practice for LAT error ellipses), and thus underestimate the true error on the position determinations. This is predominately because our span include only 1.5 periods of the annual sinusoid induced by an error in the position. Timing instabilities present on a similar timescale can thus perturb the fitted position. In addition, there are strong covariances between the astrometric and spin parameters that mean that the parameters are not actually determined to as high a precision as indicated by the 1-parameter statistical errors. Because knowing the true positional uncertainties is very important for counterpart searches at other wavelengths, we have tried to quantify the magnitude of this effect by Monte Carlo simulation. We make the assumption that over the short span of data we have, the measured values of $\ddot{\nu}$ and $\ddot{\nu}$ are dominated by timing noise, not the secular spindown of the pulsar. To estimate the magnitude of the systematic error, we generate many simulated sets of TOAs, each one using the measured timing parameters for the pulsar, with the exception of $\ddot{\nu}$ and $\ddot{\nu}$. For those two parameters, we replace them with normally-distributed random values with mean zero and standard deviation equal to the measured value, or the upper limit in the case where $\ddot{\nu}$ is not significantly detected. For ν and $\dot{\nu}$ we use random values distributed around the measured value with the measured uncertainty. Each trial set of TOAs is then fit with a 1-year sine wave plus a polynomial up to order $\ddot{\nu}$ (see Figure 3) and the magnitude of the sine wave is converted to a position offset (see Appendix A). We then compute the position uncertainty by finding the position offset that 68% of the trials are lower than. It is important to note that our simulations include random, uncorrelated, measurement errors as appropriate for the particular pulsar, so these position error estimates are of the *total* uncertainty, including both systematic and statistical components. Also, the fidelity of the estimates depends on how well our random polynomial model of the timing noise describes the actual situation, which is not well understood and may vary from pulsar to pulsar. Therefore, these estimates should be considered indicative of the

⁶See http://fermi.gsfc.nasa.gov/ssc/library/support/psr_tools_anatomy/

⁷<http://tempo2.sourceforge.net/>

⁸<http://fermi.gsfc.nasa.gov/ssc/data/analysis/user/>

magnitude of the position error, but not precise bounds on the systematic errors. Finally, in this analysis, we just consider the total position offset, so it yields an intermediate value in the cases where the position error region from the timing is highly elliptical.

For all timing models we use the JPL DE405 planetary ephemeris (Standish 1998). All reported frequencies and epochs are referenced to the TDB time system (Seidelmann 1992) as has been the standard for pulsar work⁹. The clock correction procedure is TT(TAI) and all fits are made with weighting by the TOA error estimates enabled (MODE 1). The reference time (TZRMJD) is for the geocenter at infinite frequency. The validity range for each model is included in the tables. Care should be taken when attempting to use these models outside of that range. In particular, models that include significant $\ddot{\nu}$ or higher order derivatives, or WAVE parameters, will extrapolate very poorly outside the fit range, since timing noise is a stochastic process and neither of those parameterizations reflect a physical model of the process.

In the following subsections, we discuss some of the main results from the timing of the individual pulsars. For each pulsar, we present the timing model in a table, the post-fit timing residuals, a 2-D phaseogram, and a pulse profile. In all cases, the optimized data selections used for the pulsar timing are also used to construct the 2-D phaseogram and pulse profile figures. The phaseograms are raw photon counts and are not exposure-corrected, so the apparent variations in brightness that can be seen are from exposure variations resulting from the ~ 55 -day precession period of the spacecraft orbit, the change in rocking angle during the mission, spacecraft reboots, or automatic repoints in response to γ -ray bursts. The fluxes of γ -ray pulsars is expected to be constant on time scales of days to months.

In the discovery paper (Abdo et al. 2009a), five of the pulsars were given names of the form JHHMM+DD because the declinations were not known with sufficient precision to justify a name of the form JHHMM+DDMM. In all five

cases, we now know the position well enough to confidently add the additional precision to the names, as shown in Table 1. Also, in five cases (PSRs J1418–6058, J1741–2054, J1809–2332, J1813–1246, and J1958+2846) the current best-fit timing position would result in a different last two digits of the declination than given in the discovery paper, although in several cases we know the name to be correct based on the X-ray counterpart position. In all cases, we follow the IAU preference for not changing a source name once it is given and we continue to use the original names, except where we have only added precision, as described above. See the sections on each individual source below for a discussion of the confidence in the previously proposed counterpart associations.

3.1. PSR J0007+7303

The timing model parameters for this pulsar are displayed in Table 4 and the timing position determination, post-fit residuals, 2-D phaseogram, and folded pulse profile for this pulsar are shown in Figures 5, 6, and 7, respectively.

This was the first pulsar discovered in a blind search of γ -ray data (Abdo et al. 2008) and is believed to be the pulsar powering the compact PWN RX J0007.0+7303 near the center of the shell-type supernova remnant CTA1. As seen in Figure 5, our timing position provides independent confirmation of that conclusion. In addition, we have detected a glitch in this pulsar on 2009 May 1 with a magnitude $\Delta\nu/\nu = 5.53(1) \times 10^{-7}$, a typical glitch magnitude for a pulsar of this age. When we fit for position in the timing model, the glitch can be fully accounted for by a simple $\Delta\nu$ at the time of the glitch. However, when we hold the position fixed at the *Chandra* position of the point source (00:07:01.56, 73:03:08.3; see Halpern et al. (2004)) we find that an additional parameter is required. This can be modeled as a change in the frequency first derivative at the glitch of $\Delta\dot{\nu}/\dot{\nu}$ of 0.0010(2). It is important to note that $\ddot{\nu}$ and the glitch $\Delta\dot{\nu}$ are highly covariant and additional data will likely be required to determine whether timing noise or a frequency derivative change at the glitch are the correct model for the observed behavior. The properties of this source and the glitch will be discussed in more detail in a future paper (Abdo et al. 2011, in prep).

⁹Note that the default time system for TEMPO2 is TCB, but we override this default and use TDB as the time units for our models.

TABLE 1
PULSARS TIMED WITH THE FERMI LAT

Name	Prev. Name	Period (ms)	\dot{E} (10^{34} erg s $^{-1}$)
J0007+7303	...	315.9	45.2
J0357+3205	J0357+32	444.1	0.6
J0633+0632	...	297.4	11.9
J1124-5916	...	135.5	1195.0
J1418-6058	...	110.6	494.8
J1459-6053	J1459-60	103.2	90.9
J1732-3131	J1732-31	196.5	14.5
J1741-2054	...	413.7	0.9
J1809-2332	...	146.8	42.9
J1813-1246	...	48.1	624.1
J1826-1256	...	110.2	358.0
J1836+5925	...	173.3	1.1
J1907+0602	J1907+06	106.6	282.7
J1958+2846	...	290.0	34.2
J2021+4026	...	265.3	11.6
J2032+4127	...	143.2	27.3
J2238+5903	J2238+59	162.7	88.9

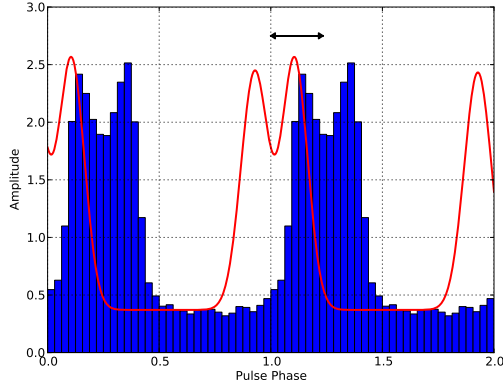


Fig. 1.— Example of a TOA measurement. The blue histogram is a binned pulse profile generated from the observed photons (two cycles are shown for clarity). The red curve is a two Gaussian template profile, where the point at phase 0.0 (or equivalently 1.0) defines the fiducial point. The black arrow represents the measured phase offset (Δ) required to align the profile with the template.

3.2. PSR J0357+3205

The timing model parameters for this pulsar are displayed in Table 5 and the timing position determination, post-fit residuals, 2-D phaseogram, and folded pulse profile for this pulsar are shown in Figures 8, 9, and 10, respectively.

PSR J0357+3205 is the slowest spin period (444 ms), and lowest \dot{E} (5.8×10^{33} erg s $^{-1}$) pulsar in our sample. In the discovery paper (Abdo et al. 2009a), it was flagged as having a potentially large systematic error in the $\dot{\nu}$ and the parameters derived from it, because of the uncertain position. The long period, low count rate, and relatively broad pulse profile still limit the timing precision to an RMS of 5.3 ms, but nevertheless the frequency derivative is now determined to an accuracy of ~ 0.2 percent.

For this low \dot{E} , the distance is constrained to be < 870 pc, assuming the flux correction factor $f_{\Omega} = 1$ (Watters et al. 2009) and using the LAT γ -ray flux (G_{100}) from Abdo et al. (2010d) to keep the γ -ray efficiency < 1 . As seen in Figure 8, no X-ray counterpart is apparent in a *Swift* image of the region, which is not surprising in such a

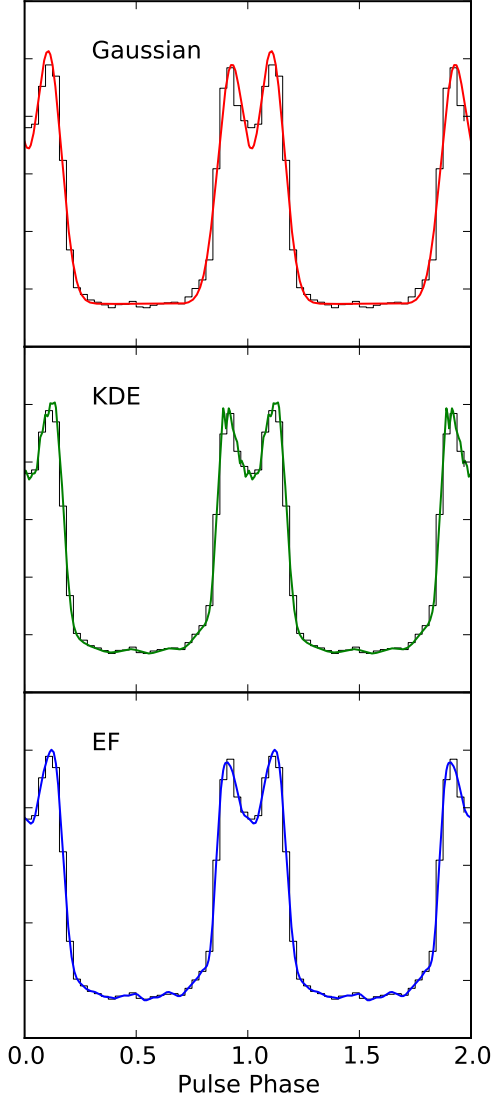


Fig. 2.— The pulse profile of PSR J0007+7303 fitted with a 2 Gaussian, Kernel Density Estimator (KDE), and Empirical Fourier (EF) template with 16 harmonics. The black histogram shows the measured pulse profile with 32 bins, but the templates are fitted to the unbinned photon phases, as described in the text

shallow exposure. However, as the pulsar is at such a small distance, this is a promising target for deeper *XMM-Newton* or *Chandra* follow up. Using the TEMPO2 simulation capability, we predict a $1\text{-}\sigma$ uncertainty on the timing position of $2''$ after 5 years of observation.

3.3. PSR J0633+0632

The timing model parameters for this pulsar are displayed in Table 6 and the timing position determination, post-fit residuals, 2-D phaseogram, and folded pulse profile for this pulsar are shown in Figures 11, 12, and 13, respectively.

This pulsar is also rather slow (297 ms) and faint (only 815 photons detected per year), but the timing is still quite good (RMS = 1.4 ms), as a result of the very narrow pulses. The timing localization is close to the X-ray point source Swift J063343.8+063223 which was proposed as the counterpart by Abdo et al. (2009a).

To further study the X-ray counterpart, we obtained a 20 ks *Chandra* ACIS-S image of the region on 2009 December 11 (ObsID 11123). The X-ray point source counterpart to the pulsar is clearly visible in Figure 11. We measure a position of 06:33:44.142, +06:32:30.40, which is $4.6''$ from the best fit timing position. To fit the spectrum of this source, we analyzed the data using CIAO version 4.3 with the latest calibrations (CALDB 4.1.1) applying the standard particle background subtraction and exposure correction. We extracted 326 photons from a 3.5 pixel extraction region around the source location (for a count rate of 1.63×10^{-2} cts s^{-1}). We see no evidence for a compact (arcsecond-scale) PWN in the immediate vicinity of the point source. To fit the spectrum, we found that an absorbed blackbody + powerlaw model is required. We obtain the following parameters from our fits, with 90% confidence error estimates: $n_H = 0.15^{+0.16}_{-0.10} \times 10^{22} \text{ cm}^{-2}$, $kT = 0.11^{+0.03}_{-0.02} \text{ keV}$, $\Gamma = 1.5 \pm 0.6$. This model yields a 0.5–8 keV flux estimate of $9.2^{+1.8}_{-1.2} \times 10^{-14} \text{ erg cm}^{-2} \text{ s}^{-1}$. If we instead fit an absorbed neutron star atmosphere (*nsa*; Zavlin et al. (1996)) plus powerlaw model, we find a somewhat higher n_H of $0.24^{+0.12}_{-0.21} \times 10^{22} \text{ cm}^{-2}$, a lower temperature of $kT = 0.048^{+0.019}_{-0.016} \text{ keV}$, and a similar photon index $\Gamma = 1.39^{+0.6}_{-0.3}$.

To look for larger-scale extended emission, we

smoothed the Chandra image with a gaussian kernel of $1.5''$ width (see Figure 4) and find a faint X-ray nebula extending about an arcminute south of the pulsar. In the region of the PWN (as shown in the Figure 4), we find an excess of 738 counts on a background of about 1600 counts and have fit the integrated spectrum with an absorbed powerlaw model. With all parameters free, we find $n_H = 0.1^{+0.3}_{-0.1} \times 10^{22} \text{ cm}^{-2}$, $\Gamma = 0.9^{+0.5}_{-0.4}$ for a flux in the 0.5–8 keV band of $2.2 \pm 0.5 \times 10^{-13} \text{ erg cm}^{-2} \text{ s}^{-1}$, where the error regions are at the 90% confidence level. If instead, we freeze n_H at $0.154 \times 10^{22} \text{ cm}^{-2}$, as found in the blackbody + powerlaw spectral fits of the point source, we find a 90% confidence range for the photon spectral index Γ of 0.74–1.29.

3.4. PSR J1124–5916

The timing model parameters for this pulsar are displayed in Table 7 and the timing position determination, post-fit residuals, 2-D phaseogram, and folded pulse profile for this pulsar are shown in Figures 14, 15, and 16, respectively.

This pulsar with very small characteristic age ($\tau_c = P/2\dot{P} = 2900 \text{ yr}$) is associated with the supernova remnant G292.0+1.8 and is the only one in this sample that was previously known as a radio pulsar (Camilo et al. 2002). It has a very high \dot{E} of $1.2 \times 10^{37} \text{ erg s}^{-1}$ and exhibits a great deal of timing noise. It is also very faint, with a 1.4 GHz flux density of only 0.08 mJy (Camilo et al. 2002) and far enough south that it can only be timed with the Parkes Telescope, where it requires several hours of integration to even get a detection. Therefore, it has not been regularly timed with radio observations since its discovery. Because there was no contemporaneous radio ephemeris available, the LAT pulsations from this source were discovered using a limited blind search around the known spin parameters. With our LAT timing, we are able to obtain TOA uncertainties of 1.5–3.2 ms every two weeks and obtain a phase-connected timing model. The timing position is $1.8''$ from the *Chandra* source CXOU J112439.1–591620 (Camilo et al. 2002). The pulsar exhibited a glitch of magnitude $\Delta\nu/\nu = 1.6 \times 10^{-8}$ around MJD 55191. A small $\Delta\dot{\nu}/\dot{\nu}$ of $-0.00472(3)$ was also observed at the glitch.

The very large measured $\ddot{\nu}$ results in a Monte

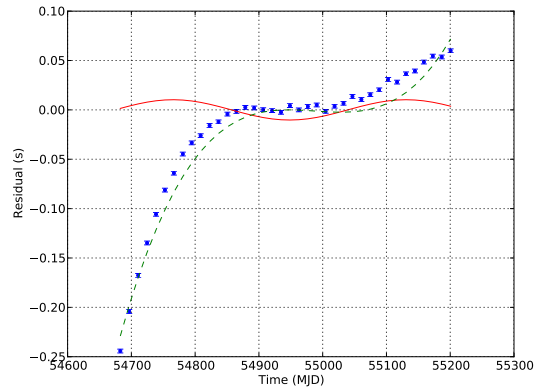


Fig. 3.— Example of a Monte Carlo trial to estimate the systematic error on the timing position. The blue points with error bars are the simulated TOAs, which are fitted to the sum of a 1-year sinusoid (solid red line) and a third order polynomial (dashed green line), as described in the text.

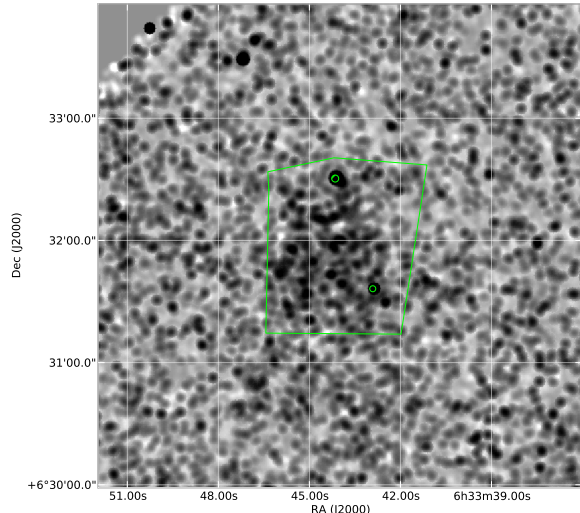


Fig. 4.— Chandra 0.5–7 keV ACIS-S image of PSR J0633+0632, smoothed with a gaussian of 3 pixels (at a scale of $0.5''$ per pixel) to highlight the extended PWN emission. The extraction region used for the PWN spectral analysis is shown, where the two point sources are excluded from the region. The pulsar is the northernmost of the two point sources in the region.

Carlo position error estimate of about $1'$, but given the good agreement between the timing position and the Chandra position, this must be a large overestimate, perhaps because the assumptions inherent in the Monte Carlo estimate are violated. The measured $\ddot{\nu}$ results in a braking index $n = \frac{\nu\ddot{\nu}}{\dot{\nu}^2} = -3.78$, which is of comparable magnitude, but *opposite* in sign to the $n = 3$ expected for vacuum dipole braking (Lorimer & Kramer 2005). This measurement, along with the substantial red noise still present in the timing residuals (see Figure 15) all suggest that the spindown of this pulsar is rather noisy.

To measure the radio to γ -ray phase alignment of this pulsar, we made a 5-hour observation with the Parkes Radio Telescope at a frequency of 1.4 GHz. Since this pulsar is not timed routinely in the radio, we required a new, contemporaneous, observation because the extreme timing noise in this system prevents the timing model from being extrapolated forward or backwards in time. This radio light curve was presented previously in the First Fermi LAT Catalog of Gamma-ray Pulsars (Abdo et al. 2010d), but the absolute phase alignment presented there was incorrect. The version presented here correctly accounts for the delay from interstellar dispersion using $DM = 330$ pc cm $^{-3}$. The new value for the lag from the radio peak to the first γ -ray peak (δ) is 0.128(3). This correction was also made to the catalog in an erratum (Abdo et al. 2011).

3.5. PSR J1418–6058

The timing model parameters for this pulsar are displayed in Table 8 and the timing position determination, post-fit residuals, 2-D phaseogram, and folded pulse profile for this pulsar are shown in Figures 17, 18, and 19, respectively.

In the discovery paper this pulsar was proposed to be associated with the PWN G313.3+0.1 (“The Rabbit”). Ng et al. (2005) find two point sources (R1 and R2) in *Chandra* and XMM observations of the region. Recently, Roberts (2009) reported a weak detection of X-ray pulsations at the period of PSR J1418–6058 in XMM data, so it is believed that R1 is the correct counterpart. However, the timing position is $14''$ from the position of R1 (RA. = 14:18:42.7, Decl. = $-60:58:03$), which is significantly larger than the $2''$ statistical error on the position. It is important to note that this pulsar is

very noisy and the timing model, which includes terms up to the frequency third derivative, clearly does not fully describe the data (see Figures 18 and 19). This causes the statistical error to be underestimated and there is a significant systematic error on the position as well. For example, adding a fourth frequency derivative to the model causes the position to shift by $10''$. As seen in Figure 17, there are three X-ray point sources near the nominal timing position, but none are coincident with the timing position. The X-ray point source R2 is not apparent in this image, so it is likely variable, and probably not the counterpart to the pulsar. A Monte Carlo estimation of the systematic error (see §3) on the position induced by the timing noise seen in this pulsar is $7''$ for the polynomial model for timing noise and $40''$ using the red noise model with an RMS of 62 ms (as computed from the measured $\dot{\nu}$ and $\ddot{\nu}$ for the pulsar). Therefore, we can’t exclude R1 as being the counterpart based on the positional disagreement. In addition, the faint X-ray source just north of the pulsar, which we call CXOU J141843.3-605734, is equally consistent with the timing and so further data, or a confirmation of the X-ray pulsations from R1, will be required to confirm the association with either source.

3.6. PSR J1459–6053

The timing model parameters for this pulsar are displayed in Table 9 and the timing position determination, post-fit residuals, 2-D phaseogram, and folded pulse profile for this pulsar are shown in Figures 20, 21, and 22, respectively.

In the discovery paper, no counterpart was known for this pulsar. With the high precision timing now available, we see that the *Swift* image shows an apparent faint point source near ($9.8''$ offset from) the timing position (see Figure 20). We call this source Swift J145931.3–605319, but its properties are not well constrained because of the faintness in the 6 ks *Swift* image. A deeper X-ray image is required to confirm this source.

3.7. PSR J1732–3131

The timing model parameters for this pulsar are displayed in Table 10 and the timing position determination, post-fit residuals, 2-D phaseogram, and folded pulse profile for this pulsar are shown

in Figures 23, 24, and 25, respectively.

This source shows minimal timing noise, with only an upper limit of $2 \times 10^{-23} \text{ s}^{-3}$ on $|\ddot{\nu}|$. The timing error ellipse is significantly elongated because of the low ecliptic latitude of the source ($\beta = -8.2^\circ$), causing the declination to be more poorly constrained than the R.A. Earlier *Swift* imaging showed no significantly-detected X-ray source at the pulsar location, so we pursued a deeper observations with *Chandra*. Our 20 ks *Chandra* ACIS-S image (ObsID 11125) reveals an X-ray point source consistent with the timing position (see Figure 23). We measure the position as 17:32:33.551, $-31:31:23.92$, which is $0.9''$ from the timing position, well within the 95% confidence region.

We performed a spectral analysis of the source based on 79 photons from the point source (with $\lesssim 1$ count from the background). Since the source is still detected even with a low energy cut of 3.5 keV, it is clear that a non-thermal component is required. However, with the small number of counts, the power law photon index cannot be constrained, so we freeze it at $\Gamma = 1.5$ in the fits. The spectral parameters from our fits to an absorbed blackbody + powerlaw are (with 90% confidence error regions) $n_H = 0.22^{+0.50}_{-0.22} \times 10^{22} \text{ cm}^{-2}$, $kT = 0.19^{+0.20}_{-0.07} \text{ keV}$. The implied 0.5–8 keV flux estimate is $(2.8 \pm 0.7) \times 10^{-14} \text{ erg cm}^{-2} \text{ s}^{-1}$ with the error at the 68% confidence interval. This corresponds to an unabsorbed flux of $4 \times 10^{-14} \text{ erg cm}^{-2} \text{ s}^{-1}$.

3.8. PSR J1741–2054

The timing model parameters for this pulsar are displayed in Table 11 and the timing position determination, post-fit residuals, 2-D phaseogram, and folded pulse profile for this pulsar are shown in Figures 26, 27, and 28, respectively.

The bright X-ray counterpart (Swift J174157.6–205411) seen in Figure 26 was proposed as the likely counterpart to this pulsar in the discovery paper. Subsequently, a LAT timing position presented by Camilo et al. (2009), who also reported the discovery of radio pulsations from this pulsar, added confidence to this proposal, and the model we present here strengthens the case. The position error is still highly elongated in the declination direction because of the very low ecliptic latitude

of the source. The X-ray source properties are studied in detail in Camilo et al. (2009). The larger span of data included in this model results in significantly more counts in the light curve, confirming the apparent 3-peak nature as proposed by Camilo et al. (2009), in contrast to the peak multiplicity of 2 assigned by Abdo et al. (2010d).

3.9. PSR J1809–2332

The timing model parameters for this pulsar are displayed in Table 12 and the timing position determination, post-fit residuals, 2-D phaseogram, and folded pulse profile for this pulsar are shown in Figures 29, 30, and 31, respectively.

This pulsar was discovered in the direction of the Galactic unidentified γ -ray source GeV J1809–2327. *Chandra* observations revealed a probable pulsar with PWN that was proposed as the source of the γ -rays (Braje et al. 2002). The point source, CXOU J180950.2–233223, was assumed as the counterpart by Abdo et al. (2009a). As seen in Figure 29, the position error ellipse is very strongly elongated, again because of the very low ecliptic latitude of the source. Nevertheless, the X-ray point source is within the timing error ellipse, strengthening the identification with this point source. If the TOAs are fitted with the position held fixed at the location of the *Chandra* point source, there are significant correlated residuals, which require a frequency third derivative term in the model to give a reasonable χ^2 for the fit.

3.10. PSR J1813–1246

The timing model parameters for this pulsar are displayed in Table 13 and the timing position determination, post-fit residuals, 2-D phaseogram, and folded pulse profile for this pulsar are shown in Figures 32, 33, and 34, respectively.

This pulsar, which has the highest spindown luminosity of the first 16 blind search pulsars discovered with the LAT, exhibited a glitch on about 2009 September 20 with magnitude $\Delta\nu/\nu = 1.17 \times 10^{-6}$. The timing model for the glitch presented here represents the data fairly well, but is not unique. Our model includes an instantaneous and permanent jump in the pulsar frequency and frequency derivative at the glitch. Other solutions are possible with slightly different glitch epochs

(within a day or so) and different parameters, or with decaying transient changes in the spin parameters at the glitch. With 6 days between TOA measurements and significant timing noise seen in this pulsar, we are not able to distinguish between these possibilities. It is clear in Figure 33 that there are significant non-white residuals remaining in the data, indicating that the model is not fully accounting for the spindown behavior of the pulsar. With a longer span of post-glitch data a more definitive model may be possible.

The bright X-ray source, Swift J181323.4–124600, was noted as the counterpart to this pulsar in the discovery paper and our timing confirms the association.

3.11. PSR J1826–1256

The timing model parameters for this pulsar are displayed in Table 14 and the timing position determination, post-fit residuals, 2-D phaseogram, and folded pulse profile for this pulsar are shown in Figures 35, 36, and 37, respectively.

The fast spin and narrow pulse profile allow this pulsar to be localized to about $1''$. The timing position is consistent with the X-ray point source AX J1826.1–1257 (R.A. = 18:26:08.2, Decl. = $-12:56:46$), which was discovered in ASCA observations of the EGRET γ -ray source GeV J1825–1310 (Roberts et al. 2001). An improved position of the X-ray point source (R.A. = 18:26:08.54, Decl. = $-12:56:34.6$) was derived from a Chandra image (M. Roberts, private communication), which is $1.6''$ from the timing position. The measured $\dot{\nu}$ for this pulsar is quite large, and the Monte Carlo error estimate yields $17''$, which is much larger than the offset seen between the timing position and the X-ray counterpart.

3.12. PSR J1836+5925

The timing model parameters for this pulsar are displayed in Table 15 and the timing position determination, post-fit residuals, 2-D phaseogram, and folded pulse profile for this pulsar are shown in Figures 38, 39, and 40, respectively.

A detailed analysis and earlier timing model for this source were published by Abdo et al. (2010a). Our model, which includes an additional 6 months of data is consistent with the earlier results with the addition of a weak detection of a frequency

second derivative term. As seen in Figure 38, the timing position is fully consistent with the X-ray source RX J1836.2+5925, with the offset being only $0.2''$.

3.13. PSR J1907+0602

The timing model parameters for this pulsar are displayed in Table 16 and the timing position determination, post-fit residuals, 2-D phaseogram, and folded pulse profile for this pulsar are shown in Figures 41, 42, and 43, respectively.

A detailed analysis of this pulsar, including an earlier timing solution and the discovery of radio pulsations, was presented by Abdo et al. (2010c). Our timing model is fully consistent within the errors to the one they presented, though we now have almost 5 months more data, which significantly reduces the uncertainties in the parameters. The position reported for the *Chandra* point source is $2.3''$ from our best timing position, which is significantly larger than the $0.6''$ statistical error in the timing position or the $0.6''$ error in the *Chandra* position. However, the offset is comparable to the expected systematic error from timing noise, based on the Monte Carlo simulations, so this is not strong evidence against the association.

3.14. PSR J1958+2846

The timing model parameters for this pulsar are displayed in Table 17 and the timing position determination, post-fit residuals, 2-D phaseogram, and folded pulse profile for this pulsar are shown in Figures 44, 45, and 46, respectively.

In the discovery paper (Abdo et al. 2009a), the X-ray source Swift J195846.1+284602 was proposed as the likely counterpart and used for the name of the pulsar. As shown in Figure 44, the timing position no longer supports this identification, being offset from the X-ray source by $80''$. There is no significant X-ray counterpart detected at the timing position. There is also no indication for strong timing noise in this pulsar, which might cause a large systematic error in the timing position. Deeper X-ray observations will be required to detect the true X-ray counterpart for this source.

3.15. PSR J2021+4026

The timing model parameters for this pulsar are displayed in Table 18 and the timing position determination, post-fit residuals, 2-D phaseogram, and folded pulse profile for this pulsar are shown in Figures 47, 48, and 49, respectively.

PSR J2021+4026 is the long-sought pulsar in the γ Cygni supernova remnant (SNR G78.2+2.1). In the discovery paper (Abdo et al. 2009a), it was pointed out that the X-ray source S21, as identified earlier in Chandra observations (Weisskopf et al. 2006), was the most likely counterpart based on the initial pulsar timing. Our best fit position is $7.7''$ to the west of S21 (see Figure 47), an offset that is somewhat larger than the predicted systematic error of $2.5''$ based on our Monte Carlo. However, when $\ddot{\nu}$ is added to the model, the position shifts by $4.6''$, so this is a lower bound on the systematic error from the timing noise. As S21 is still the closest X-ray source to the timing position, we conclude that it is indeed the likely counterpart. Longer term timing will improve our localization and reduce the systematic error contribution from timing noise. A similar conclusion was reached by Trepl et al. (2010).

Both the timing position and the X-ray source S21 are well outside the 95% confidence localization ellipse of the LAT sources, as seen in Figure 47. However, this region includes statistical errors only and this source is in the very complicated Cygnus region of the Galaxy. The localization of 0FGL J2021.5+4026 in the LAT Bright Source List (Abdo et al. 2009b) did include S21, but with the improved statistics using 18 months of data, systematic errors due to improperly modeled diffuse emission or unknown point sources can start to dominate the error budget. The association of the LAT source with the pulsar is beyond doubt because of the detection of pulsations.

3.16. PSR J2032+4127

The timing model parameters for this pulsar are displayed in Table 19 and the timing position determination, post-fit residuals, 2-D phaseogram, and folded pulse profile for this pulsar are shown in Figures 50, 51, and 52, respectively.

This pulsar is studied in detail by Camilo et al. (2009), who reported the discovery of radio pulsations from this source. The model presented here

is consistent with theirs, and the positional association with the *Chandra* point source MT91 213 is confirmed (see Figure 50).

3.17. PSR J2238+5904

The timing model parameters for this pulsar are displayed in Table 20 and the timing position determination, post-fit residuals, 2-D phaseogram, and folded pulse profile for this pulsar are shown in Figures 53, 54, and 55, respectively.

Even though this pulsar is quite faint, it can be timed with an RMS residual of 1 ms because of its very sharp pulse profile. Consequently, we now have a very precise timing position, but there is no significant X-ray counterpart detected in the Swift image (see Figure 53). The pulsar is located 0.6 degree from the radio pulsar J2240+5832 detected recently in γ -rays (Theureau et al. 2010). The narrow pulse profile means that this pulsar can be blanked from the LAT data with a loss of only $\sim 20\%$ of the exposure time.

4. Radio Counterpart Searches

All of these pulsars, except for PSR J1124–5916, were discovered in γ -ray searches and thus are γ -ray-selected pulsars, but targeted radio observations are required to determine if they are also radio quiet, or could have been discovered in radio surveys independently. The population statistics of radio-quiet vs. radio-loud γ -ray pulsars have important implications for γ -ray emission models (Gonthier et al. 2007). These observations are also important inputs into the population synthesis modeling of the full Galactic population of rotation-powered pulsars (Faucher-Giguère & Kaspi 2006, for example).

The precise positions derived from the LAT timing of these pulsars allowed us to perform deep follow up radio observations to search for pulsations from each of the new pulsars. We used the NRAO 100-m Green Bank Telescope (GBT), the Arecibo 305-m radio telescope, and the Parkes 64-m radio telescope for these observations. The instrument parameters used in the sensitivity calculations are shown in Table 2. The log of observations is shown in Table 3 and has columns for the target name, observation code (refer to Table 2), observation date, observation duration (t_{obs}), the R.A. and Decl. of the telescope pointing di-

rection, the offset from the true pulsar position, an estimate of the sky temperature in that direction at the observing frequency, and our computed flux density limit (S_{\min}), as described below. The observations taken from the literature have S_{\min} recomputed in a consistent way as well as the originally published flux limits in parentheses. In addition, the fluxes of the detected pulsars are noted with “Det” in parentheses. It is notable that the flux of the detected pulsar J1907+0602 is below our nominal flux limit. This is caused primarily by the fact that the detected pulsar has a much smaller duty cycle than the 10% that we assume.

All observations were taken in search mode (where all data are recorded without folding at a nominal pulse period) and the data were reduced using standard pulsar analysis software, such as PRESTO (Ransom et al. 2002). In each case, we searched a range of dispersion measure (DM) trials out to a maximum of at least 2 times the maximum DM value predicted by the NE2001 model (Cordes & Lazio 2002) for that direction. For 13 of the 16 γ -ray-selected pulsars, no radio pulsations were detected and we report upper limits in Table 3. For three of the pulsars, pulsations were detected. Pulsations from PSRs J2032+4127 and J1741–2054 were reported by Camilo et al. (2009) and very faint radio pulsations from PSR J1907+06 were reported by Abdo et al. (2010c). Here, we compile the upper limits from the literature as well as from our new observations.

We calculate upper limits in a consistent manner for all of our observations as well as those from the literature. To compute the minimum pulsar flux that would have been detected in these observations, we use the modified radiometer equation (e.g. Lorimer & Kramer 2005):

$$S_{\min} = \beta \frac{(S/N)_{\min} T_{\text{sys}}}{G \sqrt{n_p t_{\text{obs}} \Delta f}} \sqrt{\frac{W}{P - W}} \quad (6)$$

where β is the instrument-dependent factor due to digitization and other effects; $(S/N)_{\min} = 5$ is the threshold signal to noise for a pulsar to have been confidently detected; $T_{\text{sys}} = T_{\text{rec}} + T_{\text{sky}}$, G is the telescope gain, n_p is the number of polarizations used (2 in all cases); t_{obs} is the integration time; Δf is the observation bandwidth; P is the pulsar period; W is the pulse width (for uniformity, we assume $W = 0.1P$).

Because some of the observations were taken

before the precise positions were known, some of the pointing directions are offset from the true direction to the pulsar. We use a simple approximation of a telescope beam response to adjust the flux sensitivity in these cases. This factor is

$$f = \exp\left(\frac{-(\theta/\text{HWHM})^2}{1.5}\right), \quad (7)$$

where θ is the offset from the beam center and HWHM is the beam half-width at half maximum. A computed flux limit of S at the beam center is thus corrected to S/f for a target offset from the pointing direction. The resultant flux limits are compiled in Table 3.

TABLE 2
DEFINITION OF RADIO OBSERVING CODES

Obs Code	Telescope	Gain (K/Jy)	Freq (MHz)	Δf (MHz)	β^a	n_p	HWHM (arcmin)	T_{rec} (K)
GBT-350	GBT	2.0	350	100	1.05	2	18.5	46
GBT-820	GBT	2.0	820	200	1.05	2	7.9	29
GBT-820BCPM	GBT	2.0	820	48	1.05	2	7.9	29
GBT-S	GBT	1.9	2000	700 ^b	1.05	2	3.1	22
AO-327	Arecibo	11	327	50	1.12	2	6.3	116
AO-430	Arecibo	11	430	40	1.12	2	4.8	84
AO-Lwide	Arecibo	10	1510	300	1.12	2	1.5	27
AO-ALFA	Arecibo	10	1400	100	1.12	2	1.5	30
Parkes-MB256	Parkes	0.735	1390	256	1.25	2	7.0	25
Parkes-AFB	Parkes	0.735	1374	288	1.25	2	7.0	25
Parkes-BPSR	Parkes	0.735	1352	340	1.05	2	7.0	25

^aInstrument-dependent sensitivity degradation factor, see equation 6.

^bThe instrument records 800 MHz of bandwidth, but to account for a notch filter for RFI and the lower sensitivity near the band edges, we use an effective bandwidth of 700 MHz for the sensitivity calculations.

TABLE 3
RADIO OBSERVATIONS OF γ -RAY-SELECTED PULSARS

Target PSR ...	Obs Code	Date	t_{obs} (s)	R.A. ^a (J2000)	Decl. ^a (J2000)	Offset (')	T_{sky} (K)	S_{min} (μJy)
J0007+7303	GBT-820BCPM	2003 Oct 11	70560	00:07:01.6	+73:03:08	0.0	7.7	12 (22 ^b)
	GBT-S	2009 Aug 28	10000	00:07:01.6	+73:03:08	0.0	0.6	6
J0357+3205	AO-327	2009 Jan 29	7200	03:57:33.1	+32:05:03	4.1	45.7	43
	GBT-350	2010 Mar 04	1800	03:57:52.7	+32:05:19	0.0	45.7	134
J0633+0632	AO-327	2009 Jun 27	3000	06:33:32.9	+06:34:41	3.6	78.4	75
	AO-430	2009 Jan 30	4200	06:33:32.8	+06:34:40	3.6	38.5	52
	AO-Lwide	2009 Jul 03	4200	06:33:44.0	+06:32:25	0.1	1.8	3
J1418-6058	Parkes-MB256	2001 Feb 11	16900	14:18:41.5	-60:58:11	0.6	7.8	32 (80 ^c)
	Parkes-AFB	2001 Feb 13	16900	14:18:41.5	-60:58:11	0.6	7.8	30 (80 ^c)
J1459-6053	Parkes-AFB	2010 Feb 14	10200	14:59:30.0	-60:53:21	0.0	6.0	38
J1732-3131	GBT-S	2009 Aug 24	7200	17:32:33.5	-31:31:21	0.0	4.8	8
	Parkes-AFB	2009 Apr 14	16200	17:32:40.4	-31:36:35	5.4	15.5	59
J1741-2054	Parkes-AFB	2000 Nov 24	2100	17:41:51.3	-21:01:10	7.2	4.9	156 (Det 160 ^d)
J1809-2332	Parkes-BPSR	2009 Apr 15	16200	18:09:50.2	-23:32:23	0.0	10.6	26
J1813-1246	GBT-820	2009 Aug 22	5101	18:13:23.7	-12:46:15	0.0	38.9	42
	GBT-S	2009 Jan 02	3000	18:13:35.9	-12:48:05	3.6	3.0	28
J1826-1256	Parkes-MB256	2001 Feb 12	13234	18:26:04.9	-12:59:48	3.3	14.0	49 (90 ^c)
	Parkes-AFB	2001 Feb 15	14832	18:26:04.9	-12:59:48	3.3	14.0	44 (90 ^c)
	GBT-S	2010 Dec 22	10116	18:26:08.3	-12:56:34	0.0	5.5	7
	GBT-S	2011 Jan 15	9623	18:26:08.3	-12:56:34	0.0	5.5	7
J1836+5925	GBT-820BCPM	2002 Dec 06	86400	18:36:13.7	+59:25:30	0.0	5.5	10 (17 ^f)
	GBT-350	2009 Oct 24	7200	18:36:13.6	+59:25:29	0.0	50.5	70
J1907+0602	AO-ALFA	2008 Dec 04	1800	19:07:49.5	+06:01:52	1.4	8.8	22
	AO-Lwide	2009 Aug 21	3300	19:07:54.7	+06:02:16	0.0	8.8	5 (Det 3.4 ^e)
J1958+2846	AO-Lwide	2009 Oct 13	2400	19:58:40.3	+28:45:54	0.0	3.2	5
J2021+4026	GBT-S	2009 Jan 04	3600	20:21:35.6	+40:26:21	0.9	2.5	11
	GBT-820BCPM	2003 Dec 27	14400	20:21:18.1	+40:24:35	3.3	31.9	51 (40 ^g)
	GBT-820BCPM	2003 Dec 27	14400	20:21:21.5	+40:23:22	3.9	31.9	53 (40 ^g)
J2032+4127	GBT-S	2009 Jan 05	3600	20:32:13.9	+41:22:34	4.8	2.6	50 (Det 120 ^d)
J2238+5903	GBT-820	2009 Aug 22	4447	22:38:27.9	+59:03:42	0.0	12.1	27
	GBT-S	2009 Aug 24	7200	22:38:27.9	+59:03:42	0.0	0.9	7

^aTelescope pointing direction (not necessarily source position)

^bHalpern et al. (2004)

^cRoberts et al. (2002)

^dCamilo et al. (2009)
^eAbdo et al. (2010c)
^fHalpern et al. (2007)
^gBecker et al. (2004)

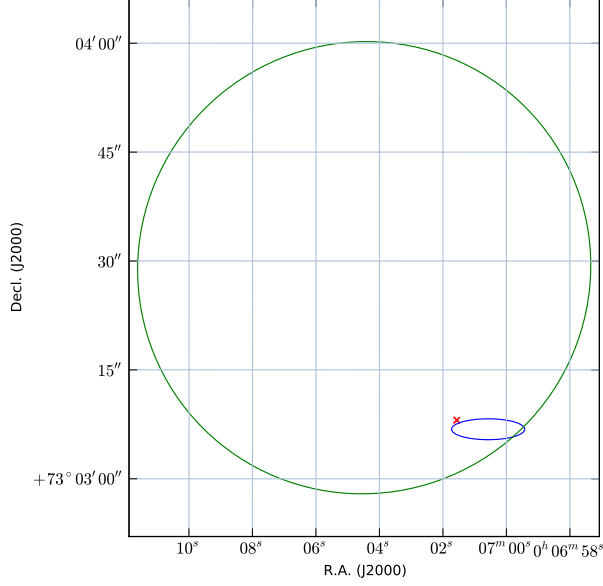


Fig. 5.— Timing position for PSR J0007+7303 (blue ellipse). The large green ellipse is the LAT 95% confidence localization of 1FGL J0007.0+7303, based on 18 months of data. The red X is the *Chandra* position of RX J0007.0+7303, which is $4.4''$ from the best timing position (Halpern et al. 2004).

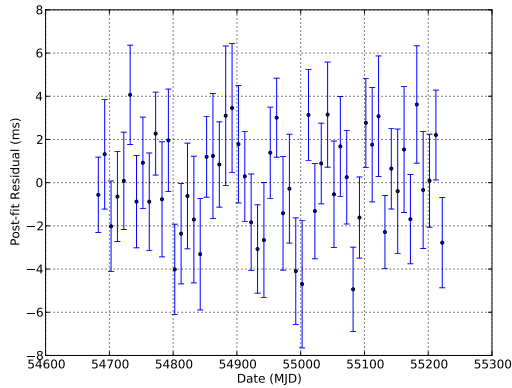


Fig. 6.— Post-fit timing residuals for PSR J0007+7303.

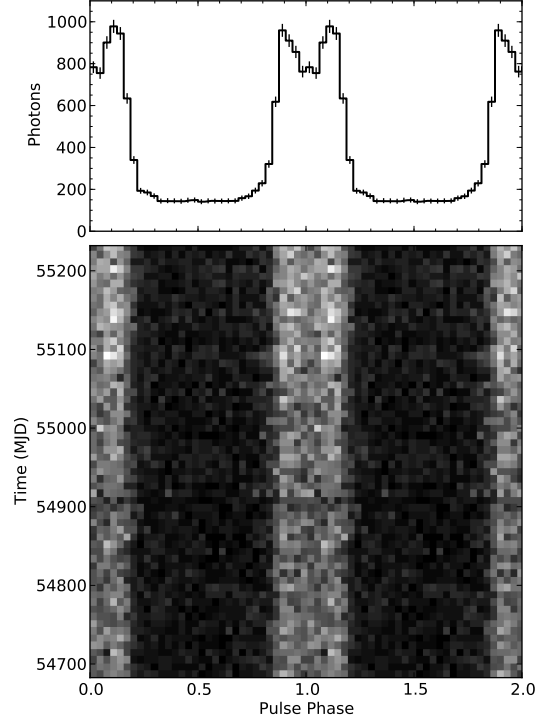


Fig. 7.— 2-D phaseogram and pulse profile of PSR J0007+7303. Two rotations are shown on the X-axis. The photons were selected according to the ROI and E_{\min} in Table 4. In this and the following phaseogram plots, the grey scale is the number of photons in each phase/time bin, without any correction for exposure, so apparent brightness changes are caused by the precession period of the *Fermi* satellite, interruptions in science operations, or from operational changes in the rocking pattern in sky survey mode. The fiducial point corresponding to TZRMJD is phase 0.0. This and all following pulse profiles are constructed with 32 bins across the pulse period.

TABLE 4
PSR J0007+7303

Parameter	Value
Right ascension, α (J2000.0).....	00:07:00.6 $\pm 0.2^s$
Declination, δ (J2000.0).....	+73:03:07.0 $\pm 0.6''$
Monte Carlo position uncertainty	2''
Pulse frequency, ν (s^{-1}).....	3.165827380(3)
Frequency first derivative, $\dot{\nu}$ (s^{-2})..	$-3.6136(2) \times 10^{-12}$
Frequency second derivative, $\ddot{\nu}$ (s^{-3})	$-7(1) \times 10^{-23}$
Epoch of Frequency (MJD)	54952
Glitch Epoch.....	54952.652
Glitch $\Delta\nu$ (s^{-1}).....	$1.759(3) \times 10^{-6}$
Glitch $\Delta\dot{\nu}$ (s^{-2}).....	0
TZRMJD	54952.334185720257651
Number of photons (n_γ)	12790
Number of TOAs	55
RMS timing residual (ms)	2.2
Template Profile	KDE
E_{\min}	150 MeV
ROI	1.5°
Valid range (MJD)	54682 – 55222

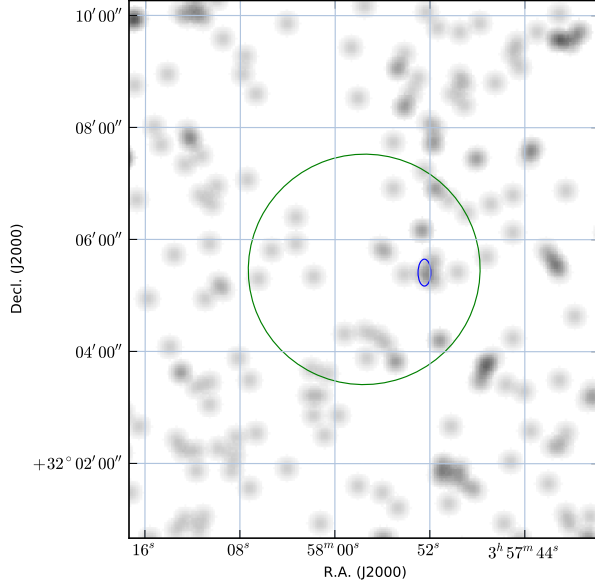


Fig. 8.— Timing position for PSR J0357+3205 (blue ellipse). The large green ellipse is the LAT position of 1FGL J0357.8+3205, based on 18 months of data. The background 0.2–10 keV X-ray image is from a 2.6 ks *Swift* observation (ObsID 00031299001), smoothed with a gaussian with $\sigma = 7''$.

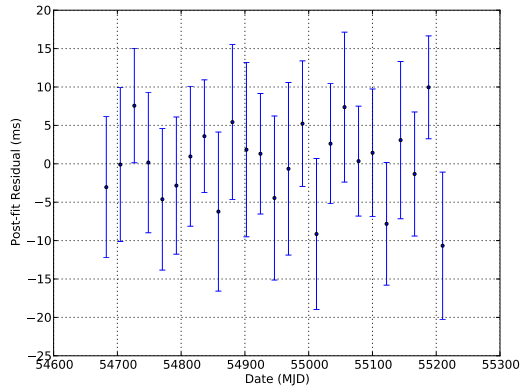


Fig. 9.— Post-fit timing residuals for PSR J0357+3205.

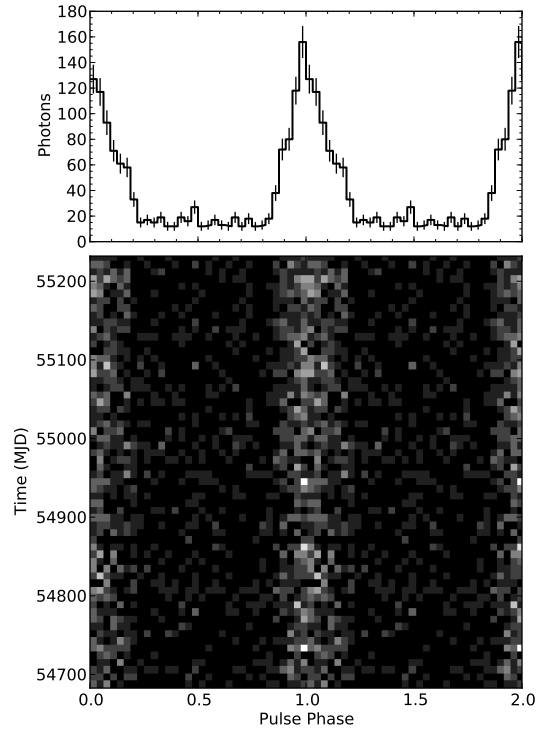


Fig. 10.— 2-D phaseogram and pulse profile of PSR J0357+3205. Two rotations are shown on the X-axis. The photons were selected according to the ROI and E_{\min} in Table 5. The fiducial point corresponding to TZRMJD is phase 0.0.

TABLE 5
PSR J0357+3205

Parameter	Value
Right ascension, α (J2000.0).....	03:57:52.5 $\pm 0.2^s$
Declination, δ (J2000.0)	+32:05:25 $\pm 6''$
Monte Carlo position uncertainty	18''
Pulse frequency, ν (s^{-1})	2.251722292(3)
Frequency first derivative, $\dot{\nu}$ (s^{-2}) ..	$-6.61(1) \times 10^{-14}$
Frequency second derivative, $\ddot{\nu}$ (s^{-3})	$ \ddot{\nu} < 6 \times 10^{-23}$
Epoch of Frequency (MJD)	54946
TZRMJD	54946.341346723796502
Number of photons (n_γ)	1335
Number of TOAs	25
RMS timing residual (ms)	5.3
Template Profile	1 Gaussian
E_{\min}	250 MeV
ROI	0.8°
Valid range (MJD)	54682 – 55210

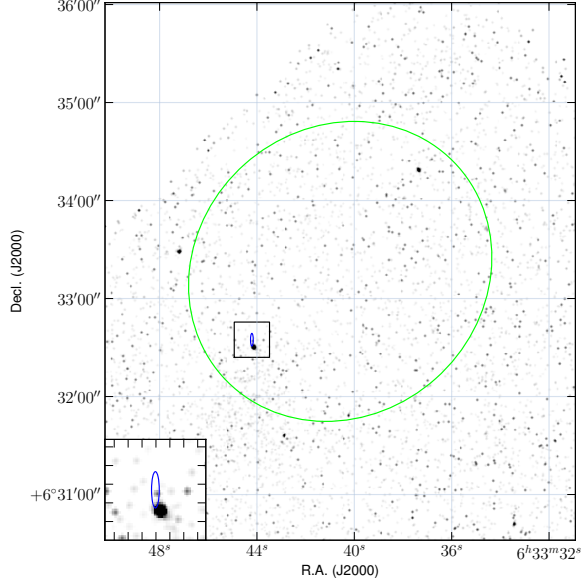


Fig. 11.— Timing position for PSR J0633+0632 (blue ellipse). The large ellipse is the LAT position of 1FGL J0633.7+0632, based on 18 months of data. The background 0.5–8 keV X-ray image is a 20 ks *Chandra* ACIS-S image (ObsID 11123), smoothed with a gaussian with $\sigma = 0.5''$. The inset shows a $10''$ region around the timing location.

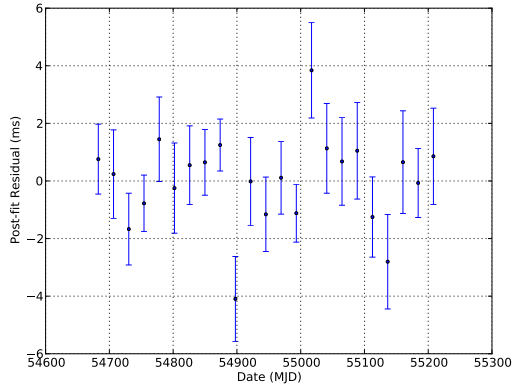


Fig. 12.— Post-fit timing residuals for PSR J0633+0632.

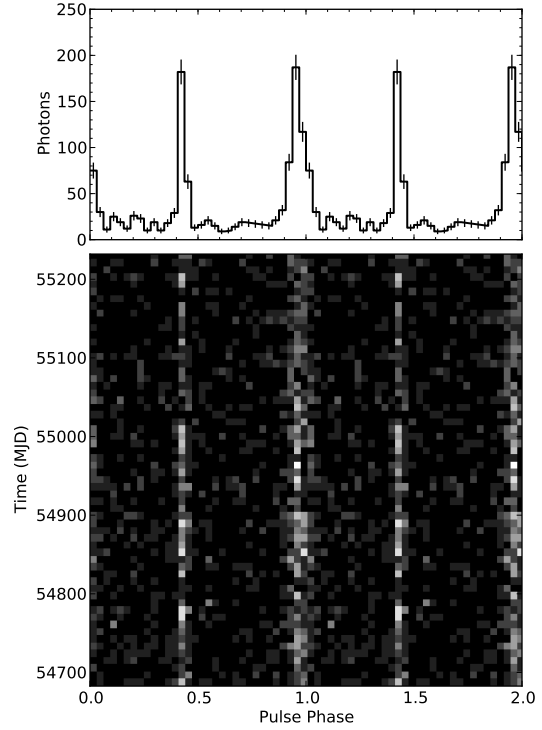


Fig. 13.— 2-D phaseogram and pulse profile of PSR J0633+0632. Two rotations are shown on the X-axis. The photons were selected according to the ROI and E_{\min} in Table 6. The fiducial point corresponding to TZRMJD is phase 0.0.

TABLE 6
PSR J0633+0632

Parameter	Value
Right ascension, α (J2000.0).....	06:33:44.21 $\pm 0.02^s$
Declination, δ (J2000.0)	+06:32:34.9 $\pm 1.6''$
Monte Carlo position uncertainty	3.5''
Pulse frequency, ν (s^{-1})	3.3625291588(7)
Frequency first derivative, $\dot{\nu}$ (s^{-2}) ..	$-8.9991(3) \times 10^{-13}$
Frequency second derivative, $\ddot{\nu}$ (s^{-3})	$-2(1) \times 10^{-23}$
Epoch of Frequency (MJD)	54945
TZRMJD	54945.385967311181439
Number of photons (n_γ)	1174
Number of TOAs	23
RMS timing residual (ms)	1.4
Template Profile	2 Gaussian
E_{\min}	550 MeV
ROI	0.6°
Valid range (MJD)	54682 – 55208

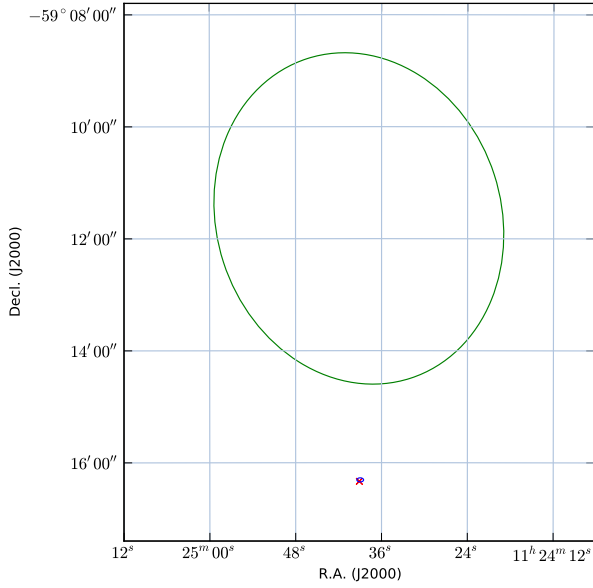


Fig. 14.— Timing position for PSR J1124–5916 (small blue ellipse). The large green ellipse is the LAT position of 1FGL J1124.6–5916, based on 18 months of data. The red cross marks the position of the Chandra point source (Camilo et al. 2002) associated with the pulsar (see §3.4).

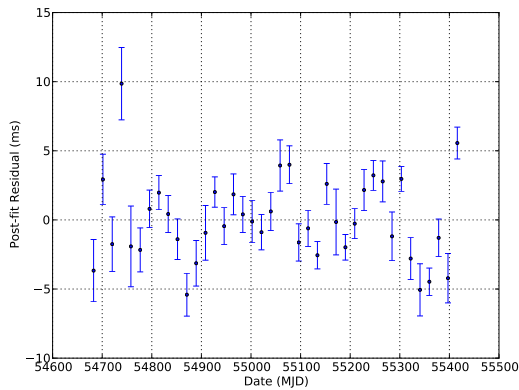


Fig. 15.— Post-fit timing residuals for PSR J1124–5916.

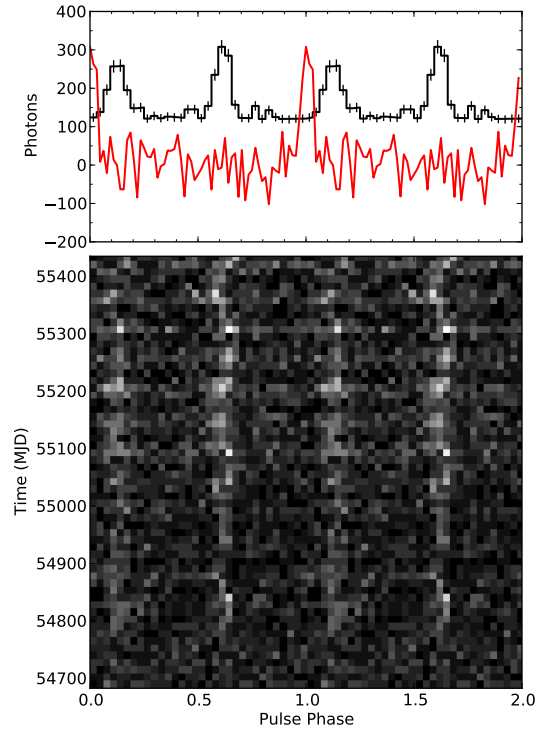


Fig. 16.— 2-D phaseogram and pulse profile of PSR J1124–5916. Two rotations are shown on the X-axis. The photons were selected according to the ROI and E_{\min} in Table 7. The fiducial point corresponding to TZRMJD is phase 0.0. The red line is a 1.4 GHz radio profile from the Parkes radio telescope, with the correct absolute phase alignment.

TABLE 7
PSR J1124–5916

Parameter	Value
Right ascension, α (J2000.0)	11:24:39.0(1)
Declination, δ (J2000.0)	−59:16:19(1)
Pulse frequency, ν (s^{-1})	7.381334652(9)
Frequency first derivative, $\dot{\nu}$ (s^{-2}) ..	$-4.10029(9) \times 10^{-11}$
Frequency second derivative, $\ddot{\nu}$ (s^{-3})	$-8.6(4) \times 10^{-22}$
Epoch of Frequency (MJD)	54683.281414
Glitch Epoch (MJD)	55191
Glitch $\Delta\nu$ (s^{-1})	$1.18(9) \times 10^{-7}$
Glitch $\Delta\dot{\nu}$ (s^{-2})	$1.94(2) \times 10^{-13}$
TZRMJD	55053.0521054597626
TZRFREQ (MHz)	1371.067
TZRSITE	7 (Parkes)
Number of photons (n_γ)	5030
Number of TOAs	40
RMS timing residual (ms)	2.8
Template Profile	2 Gaussian
E_{min}	200 MeV
ROI	0.9°
Valid range	54682–55415

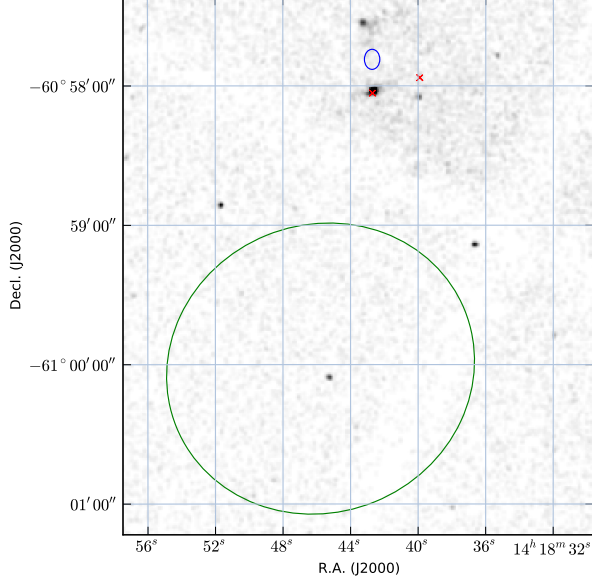


Fig. 17.— Timing position for PSR J1418–6058 (blue ellipse). The large green ellipse is the LAT position of 1FGL J1418.7–6057, based on 18 months of data. Red crosses mark the positions of the sources R1 and R2 (see §3.5). The X-ray image is a 70 ks *Chandra* ACIS observation from 2007 July 14 (ObsID 7640), first published by Roberts (2008) before the pulsar itself was detected.

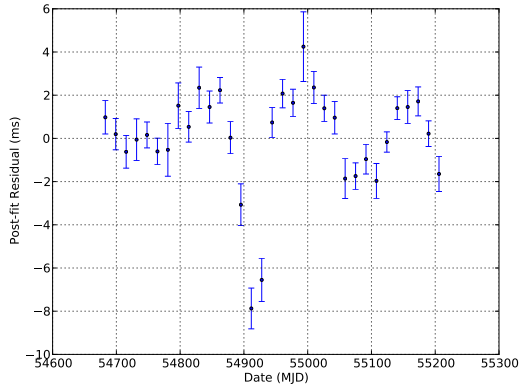


Fig. 18.— Post-fit timing residuals for PSR J1418-6058.

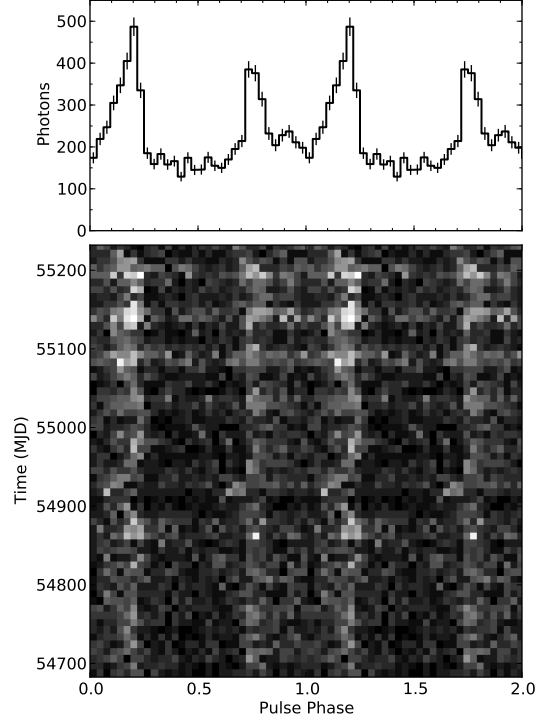


Fig. 19.— 2-D phaseogram and pulse profile of PSR J1418-6058. Two rotations are shown on the X-axis. The photons were selected according to the ROI and E_{\min} in Table 8. The fiducial point corresponding to TZRMJD is phase 0.0.

TABLE 8
PSR J1418-6058

Parameter	Value
Right ascension, α (J2000.0).....	14:18:42.7 $\pm 0.1^s$
Declination, δ (J2000.0)	-60:57:49 $\pm 2''$
Monte Carlo position uncertainty	7''
Pulse frequency, ν (s $^{-1}$)	9.043798163(1)
Frequency first derivative, $\dot{\nu}$ (s $^{-2}$) ..	-1.38548(8) $\times 10^{-11}$
Frequency second derivative, $\ddot{\nu}$ (s $^{-3}$)	6.4(3) $\times 10^{-22}$
Frequency third derivative, $\dddot{\nu}$ (s $^{-4}$).	-8(2) $\times 10^{-29}$
Epoch of Frequency (MJD)	54944
TZRMJD	54944.2886329214
Number of photons (n_γ)	7283
Number of TOAs	33
RMS timing residual (ms)	1.9
Template Profile	KDE
E_{\min}	250 MeV
ROI	0.5 $^\circ$
Valid range (MJD)	54682 - 55205

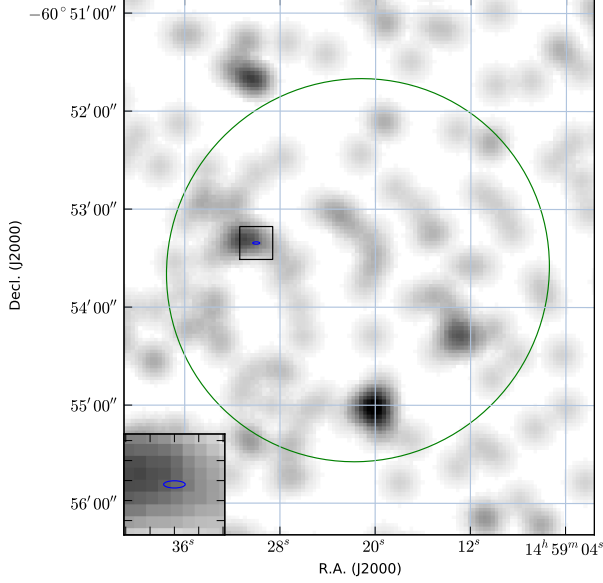


Fig. 20.— Timing position for PSR J1459–6053 (blue ellipse). The large green ellipse is the LAT position of 1FGL J1459.4–6053, based on 18 months of data. The background 0.2–10 keV X-ray image is a 6.8 ks *Swift* image (ObsID 00031359002), smoothed with a gaussian with $\sigma = 7''$. A $10 \times 10''$ region around the timing position is indicated with the black square and shown in the inset at the lower left.

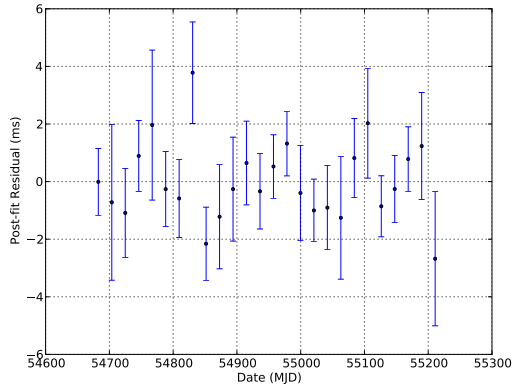


Fig. 21.— Post-fit timing residuals for PSR J1459–6053.

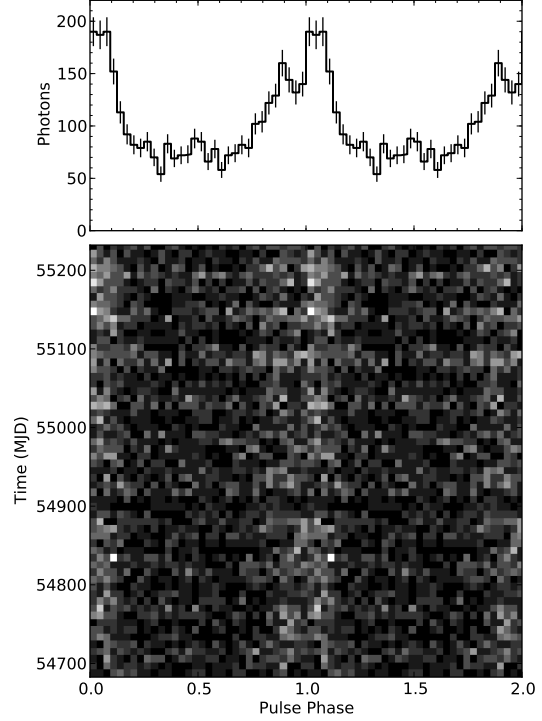


Fig. 22.— 2-D phaseogram and pulse profile of PSR J1459–6053. Two rotations are shown on the X-axis. The photons were selected according to the ROI and E_{\min} in Table 9. The fiducial point corresponding to TZRMJD is phase 0.0.

TABLE 9
PSR J1459–6053

Parameter	Value
Right ascension, α (J2000.0).....	14:59:29.99 $\pm 0.06^s$
Declination, δ (J2000.0)	-60:53:20.7 $\pm 0.4''$
Monte Carlo position uncertainty	1.3''
Pulse frequency, ν (s^{-1})	9.694559498(1)
Frequency first derivative, $\dot{\nu}$ (s^{-2}) ..	$-2.37503(5) \times 10^{-12}$
Frequency second derivative, $\ddot{\nu}$ (s^{-3})	$-4(2) \times 10^{-23}$
Epoch of Frequency (MJD)	54935
TZRMJD	54936.19962194
Number of photons (n_γ)	3305
Number of TOAs	26
RMS timing residual (ms)	1.1
Template Profile	KDE
E_{\min}	350 MeV
ROI	0.7°
Valid range (MJD)	54682–55210

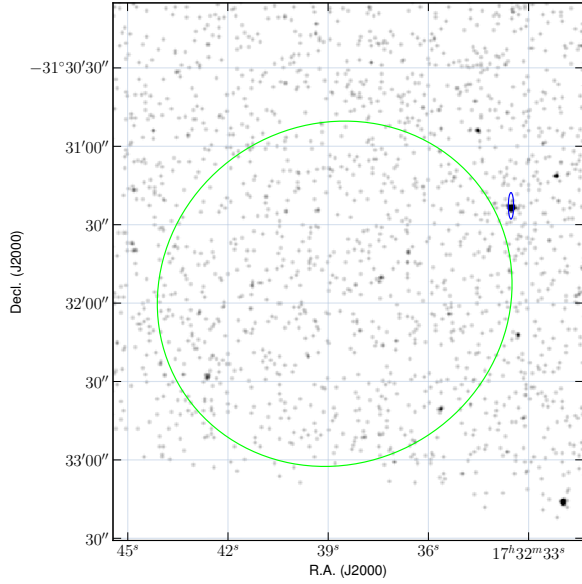


Fig. 23.— Timing position for PSR J1732–3131 (blue ellipse). The large green ellipse is the LAT position of 1FGL J1732.5–3131, based on 18 months of data. The background 0.5–8 keV X-ray image is a 20 ks *Chandra* ACIS-S image (ObsID 11125), smoothed with a gaussian with $\sigma = 0.5''$.

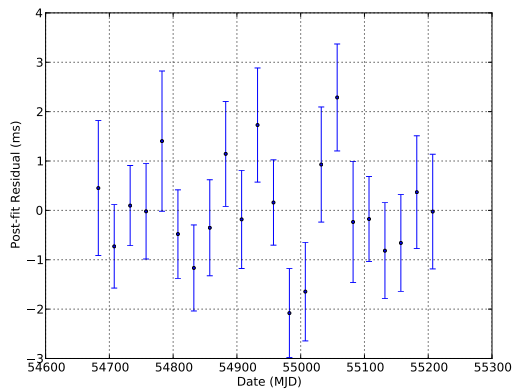


Fig. 24.— Post-fit timing residuals for PSR J1732–3131.

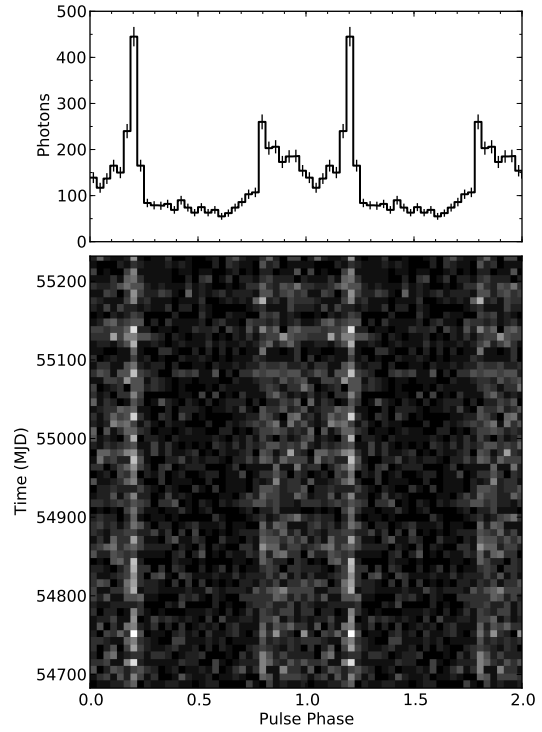


Fig. 25.— 2-D phaseogram and pulse profile of PSR J1732–3131. Two rotations are shown on the X-axis. The photons were selected according to the ROI and E_{\min} in Table 10. The fiducial point corresponding to TZRMJD is phase 0.0.

TABLE 10
PSR J1732–3131

Parameter	Value
Right ascension, α (J2000.0).....	17:32:33.54 $\pm 0.03^s$
Declination, δ (J2000.0).....	–31:31:23 $\pm 2''$
Monte Carlo position uncertainty	3''
Pulse frequency, ν (s $^{-1}$).....	5.0879411200(5)
Frequency first derivative, $\dot{\nu}$ (s $^{-2}$) ..	$-7.2609(3) \times 10^{-13}$
Frequency second derivative, $\ddot{\nu}$ (s $^{-3}$)	$ \ddot{\nu} < 2 \times 10^{-23}$
Epoch of Frequency (MJD)	54933
TZRMJD	54957.3282196892
Number of photons (n_γ)	4236
Number of TOAs	22
RMS timing residual (ms)	1.0
Template Profile	KDE
E_{\min}	400 MeV
ROI	0.5°
Valid range (MJD)	54682–55207

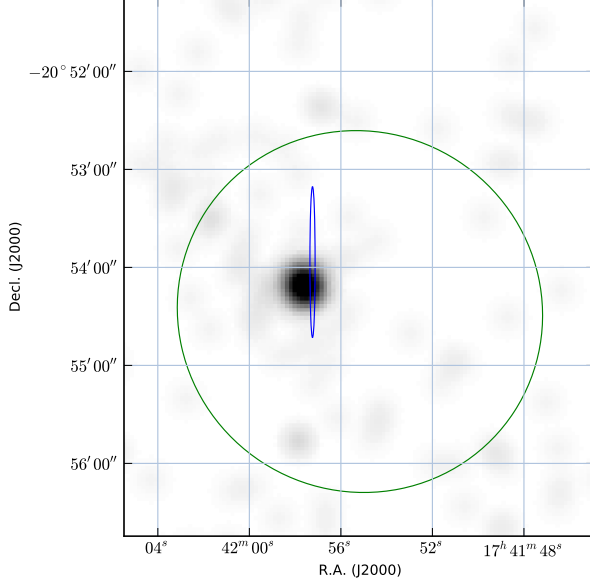


Fig. 26.— Timing position for PSR J1741–2054 (blue ellipse). The large green ellipse is the LAT position of 1FGL J1741.8–2101, based on 18 months of data. The background 0.2–10 keV X-ray image is a 4.3 ks *Swift* XRT image (ObsID 00031277001), smoothed with a gaussian with $\sigma = 7''$.

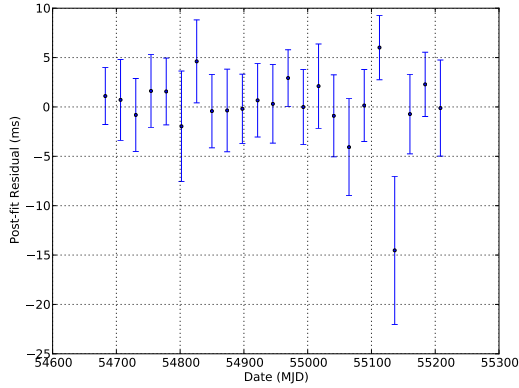


Fig. 27.— Post-fit timing residuals for PSR J1741–2054.

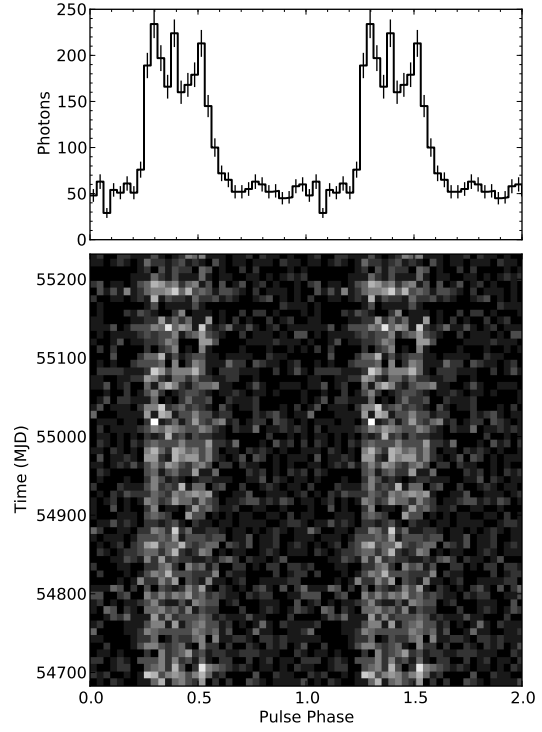


Fig. 28.— 2-D phaseogram and pulse profile of PSR J1741-2054. Two rotations are shown on the X-axis. The photons were selected according to the ROI and E_{\min} in Table 11. The fiducial point corresponding to TZRMJD is phase 0.0.

TABLE 11
PSR J1741–2054

Parameter	Value
Right ascension, α (J2000.0).....	17:41:57.23 $\pm 0.05^s$
Declination, δ (J2000.0).....	-20:53:57 $\pm 19''$
Monte Carlo position uncertainty	20''
Pulse frequency, ν (s $^{-1}$).....	2.417209833(1)
Frequency first derivative, $\dot{\nu}$ (s $^{-2}$) ..	$-9.923(3) \times 10^{-14}$
Frequency second derivative, $\ddot{\nu}$ (s $^{-3}$)	$ \ddot{\nu} < 2 \times 10^{-23}$
Epoch of Frequency (MJD)	54933
TZRMJD	54945.3859666189
Number of photons (n_γ)	3135
Number of TOAs	23
RMS timing residual (ms)	2.6
Template Profile	KDE
E_{\min}	300 MeV
ROI	0.8°
Valid range (MJD)	54682–55208

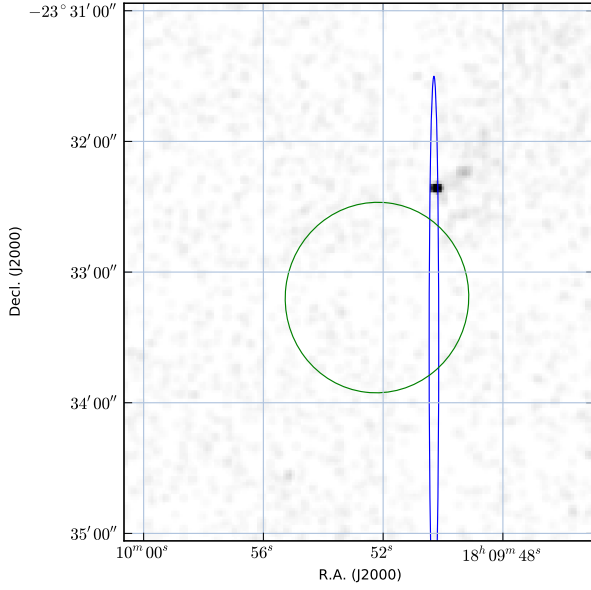


Fig. 29.— Timing position for PSR J1809–2332 (blue ellipse). The large green ellipse is the LAT position of 1FGL J1809.8–2332, based on 18 months of data. The background image is a 9.8 ks *Chandra* ACIS-I image (ObsId 739) showing the bright point source CXOU J180950.2–233223.

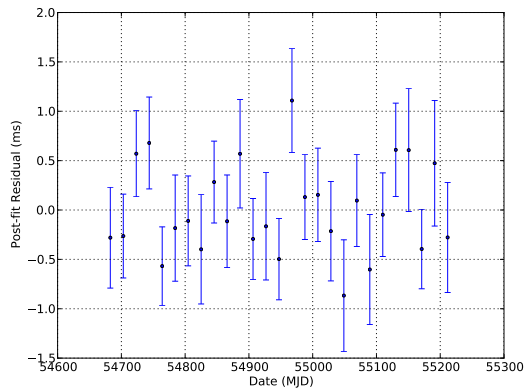


Fig. 30.— Post-fit timing residuals for PSR J1809–2332.

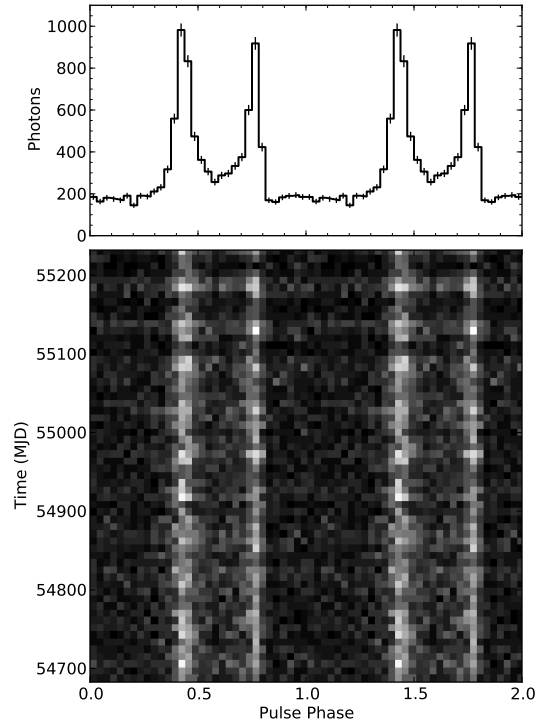


Fig. 31.— 2-D phaseogram and pulse profile of PSR J1809–2332. Two rotations are shown on the X-axis. The photons were selected according to the ROI and E_{\min} in Table 12. The fiducial point corresponding to TZRMJD is phase 0.0.

TABLE 12
PSR J1809-2332

Parameter	Value
Right ascension, α (J2000.0).....	18:09:50.31 $\pm 0.06^s$
Declination, δ (J2000.0)	$-23:33:35 \pm 51''$
Monte Carlo position uncertainty	$28''$
Pulse frequency, ν (s^{-1})	6.8125205463(3)
Frequency first derivative, $\dot{\nu}$ (s^{-2}) ..	$-1.59748(1) \times 10^{-12}$
Frequency second derivative, $\ddot{\nu}$ (s^{-3})	$ \ddot{\nu} < 1 \times 10^{-23}$
Epoch of Frequency (MJD)	54935
TZRMJD	54947.1551911038
Number of photons (n_γ)	10422
Number of TOAs	27
RMS timing residual (ms)	0.4
Template Profile	KDE
E_{\min}	250 MeV
ROI	0.8°
Valid range (MJD)	54682–55211

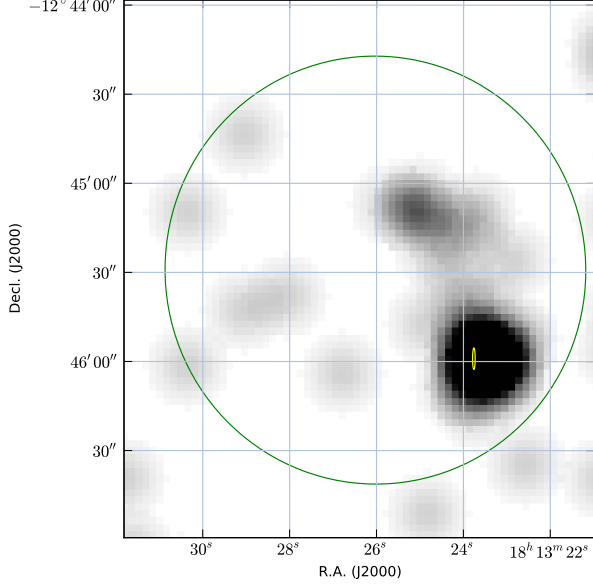


Fig. 32.— Timing position for PSR J1813-1246 (yellow ellipse). The large green ellipse is the LAT position of 1FGL J1813.3-1246, based on 18 months of data. The background X-ray image is a 3.2 ks *Swift* XRT observation (ObsID 00031381001), smoothed with a gaussian of width $7''$, showing the bright point source *Swift* J181323.4-124600.

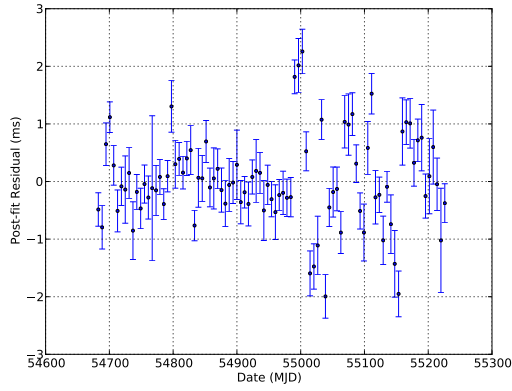


Fig. 33.— Post-fit timing residuals for PSR J1813-1246.

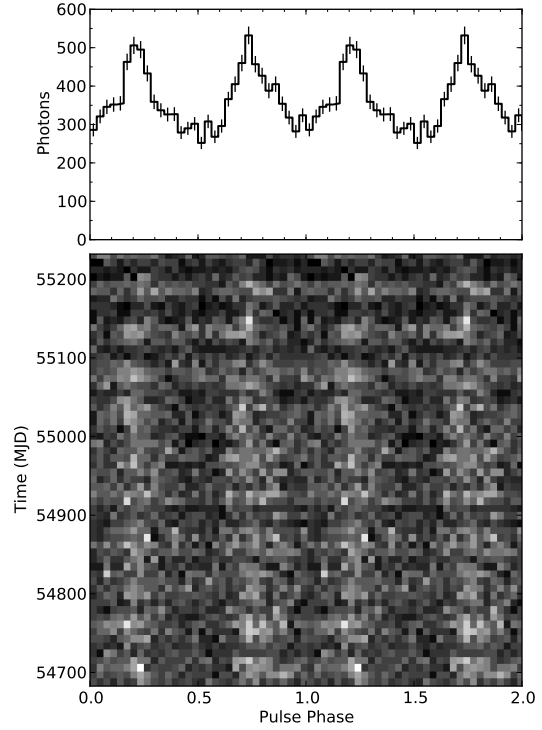


Fig. 34.— 2-D phaseogram and pulse profile of PSR J1813-1246. Two rotations are shown on the X-axis. The photons were selected according to the ROI and E_{\min} in Table 13. The fiducial point corresponding to TZRMJD is phase 0.0.

TABLE 13
PSR J1813–1246

Parameter	Value
Right ascension, α (J2000.0).....	18:13:23.77 $\pm 0.01^s$
Declination, δ (J2000.0)	–12:45:59.2 $\pm 1.5''$
Monte Carlo position uncertainty	1.5''
Pulse frequency, ν (s^{-1})	20.802023359(3)
Frequency first derivative, $\dot{\nu}$ (s^{-2}) ..	$-7.60023(9) \times 10^{-12}$
Frequency second derivative, $\ddot{\nu}$ (s^{-3})	$ \ddot{\nu} < 6 \times 10^{-23}$
Glitch Epoch.....	55094.1227
Glitch $\Delta\nu$ (s^{-1})	$2.4256(9) \times 10^{-5}$
Glitch $\Delta\dot{\nu}$ (s^{-2})	$-4.9(2) \times 10^{-14}$
TZRMJD	54954.309848738
Number of photons (n_γ)	11611
Number of TOAs	91
RMS timing residual (ms)	0.7
Template Profile	KDE
E_{\min}	200 MeV
ROI	1.0°
Valid range	54682–55226

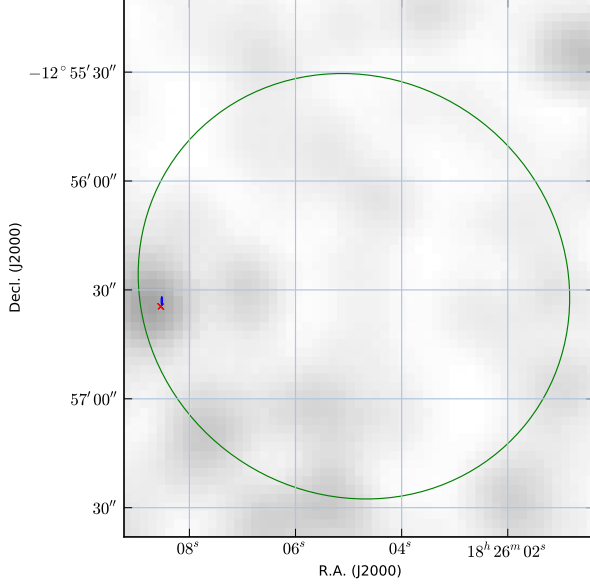


Fig. 35.— Timing position for PSR J1826-1256 (blue ellipse). The large green ellipse is the LAT position of 1FGL J1826.1-1256, based on 18 months of data. The background 0.2-10 keV X-ray image is a 4.3 ks *Swift* XRT image (ObsID 00035179002), smoothed with a gaussian with $\sigma = 7''$. The red cross marks the Chandra position of X-ray point source AX J1826.1-1257.

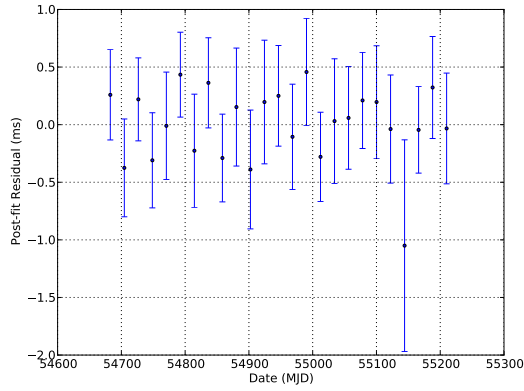


Fig. 36.— Post-fit timing residuals for PSR J1826-1256

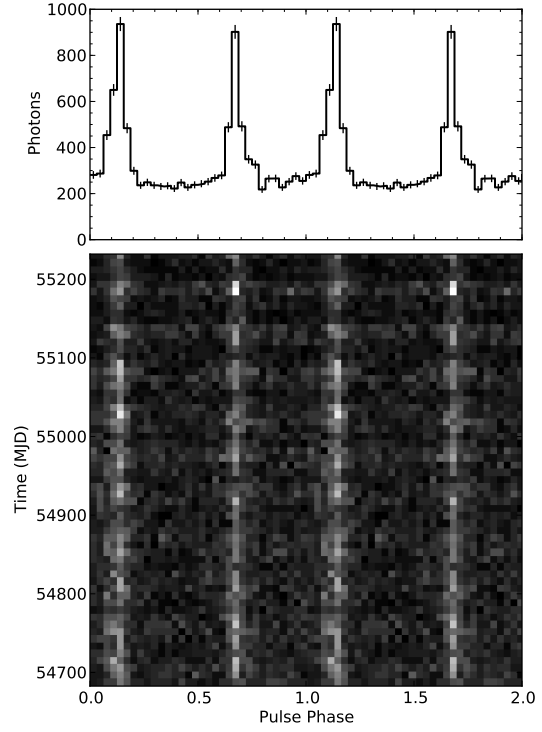


Fig. 37.— 2-D phaseogram and pulse profile of PSR J1826-1256. Two rotations are shown on the X-axis. The photons were selected according to the ROI and E_{\min} in Table 14. The fiducial point corresponding to TZRMJD is phase 0.0.

TABLE 14
PSR J1826–1256

Parameter	Value
Right ascension, α (J2000.0).....	18:26:08.53 $\pm 0.01^s$
Declination, δ (J2000.0)	$-12:56:33.0 \pm 0.5''$
Monte Carlo position uncertainty	$17''$
Pulse frequency, ν (s^{-1})	9.0724588059(3)
Frequency first derivative, $\dot{\nu}$ (s^{-2}) ..	$-9.99654(1) \times 10^{-12}$
Frequency second derivative, $\ddot{\nu}$ (s^{-3})	$1.85(5) \times 10^{-22}$
Epoch of Frequency (MJD)	54934
TZRMJD	54946.3413482956
Number of photons (n_γ)	10860
Number of TOAs	25
RMS timing residual (ms)	0.28
Template Profile	KDE
E_{\min}	200 MeV
ROI	0.6°
Valid range	54682–55210

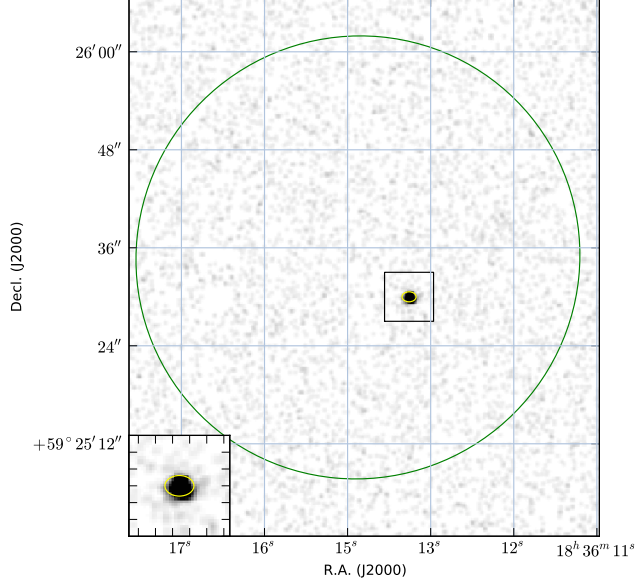


Fig. 38.— Timing position for PSR J1836+5925 (yellow ellipse). The large green ellipse is the LAT position of 1FGL J1836.2+5925, based on 18 months of data. The X-ray image is a 46 ks *Chandra* HRC image (ObsId 6182) and the point source at the timing position is RX J1836.2+5925. The inset (3.0'' in width) shows the region of the source in more detail.

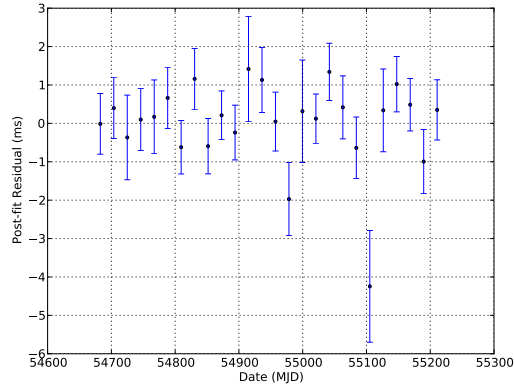


Fig. 39.— Post-fit timing residuals for PSR J1836+5925.

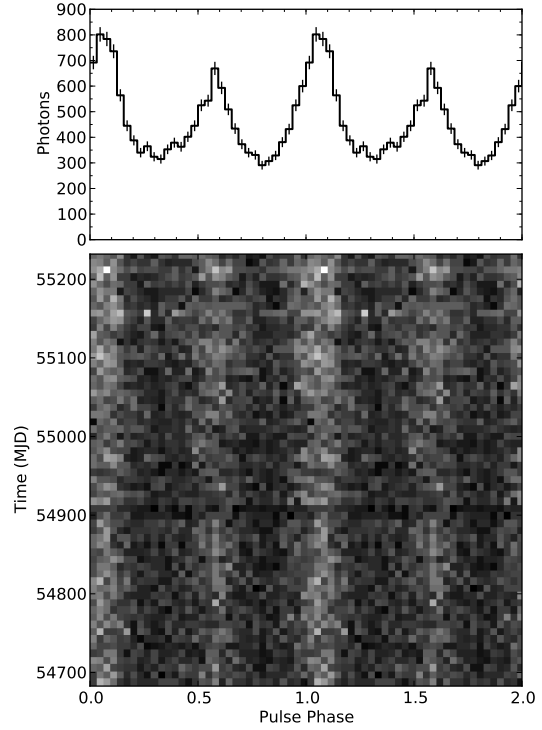


Fig. 40.— 2-D phaseogram and pulse profile of PSR J1836+5925. Two rotations are shown on the X-axis. The photons were selected according to the ROI and E_{\min} in Table 15. The fiducial point corresponding to TZRMJD is phase 0.0.

TABLE 15
PSR J1836+5925

Parameter	Value
Right ascension, α (J2000.0)	18:36:13.69 $\pm 0.02^s$
Declination, δ (J2000.0)	+59:25:30.0 $\pm 0.3''$
Monte Carlo position uncertainty	$< 3''$
Pulse frequency, ν (s^{-1})	5.7715509149(4)
Frequency first derivative, $\dot{\nu}$ (s^{-2}) ..	$-5.007(2) \times 10^{-14}$
Frequency second derivative, $\ddot{\nu}$ (s^{-3})	$-1.3(8) \times 10^{-23}$
Epoch of Frequency (MJD)	54935
TZRMJD	54936.1996219705
Number of photons (n_γ)	14875
Number of TOAs	26
RMS timing residual (ms)	0.85
Template Profile	KDE
E_{min}	200 MeV
ROI	1.6°
Valid range	54682–55210

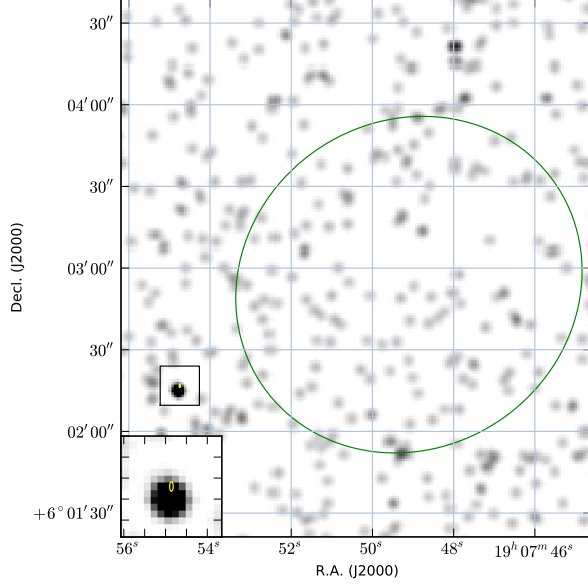


Fig. 41.— Timing position for PSR J1907+0602 (yellow ellipse). The large green ellipse is the LAT position of 1FGL J1907.9+0602, based on 18 months of data. The X-ray image is a 0.75–2.0 keV *Chandra* image (ObsID 11124). The inset (7.2'' in width) shows a detail of the region around the pulsar.

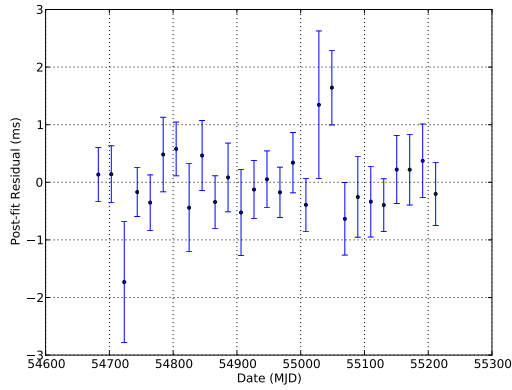


Fig. 42.— Post-fit timing residuals for PSR J1907+0602.

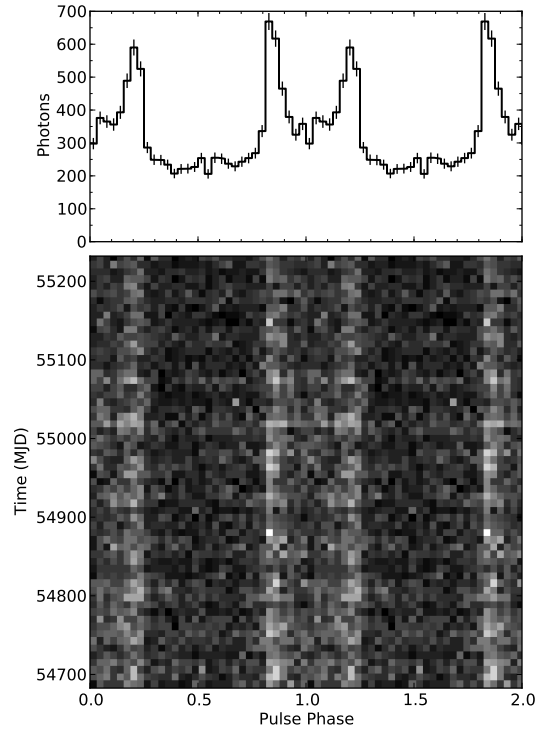


Fig. 43.— 2-D phaseogram and pulse profile of PSR J1907+0602. Two rotations are shown on the X-axis. The photons were selected according to the ROI and E_{\min} in Table 16. The fiducial point corresponding to TZRMJD is phase 0.0.

TABLE 16
PSR J1907+0602

Parameter	Value
Right ascension, α (J2000.0)	19:07:54.74 $\pm 0.01^s$
Declination, δ (J2000.0)	+06:02:16.9 $\pm 0.3''$
Monte Carlo position uncertainty	2.5''
Pulse frequency, ν (s $^{-1}$)	9.3779822336(4)
Frequency first derivative, $\dot{\nu}$ (s $^{-2}$) ..	-7.63559(2) $\times 10^{-12}$
Frequency second derivative, $\ddot{\nu}$ (s $^{-3}$)	1.88(7) $\times 10^{-22}$
Epoch of Frequency (MJD)	54935
TZRMJD	54947.1551911789
Number of photons (n_γ)	10629
Number of TOAs	27
RMS timing residual (ms)	0.47
Template Profile	KDE
E_{\min}	50 MeV
ROI	0.7 $^\circ$
Valid range	54682–55211

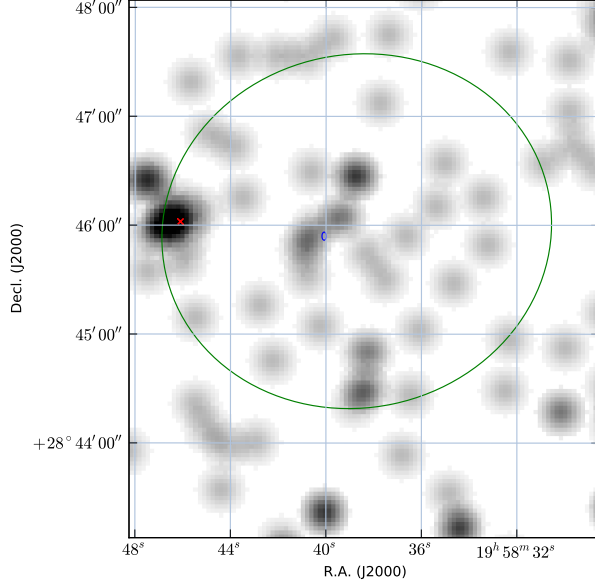


Fig. 44.— Timing position for PSR J1958+2846 (blue ellipse). The large green ellipse is the LAT position of 1FGL J1958.6+2845, based on 18 months of data. The background 0.2–10 keV X-ray image is a 5.5 ks *Swift* XRT image (ObsID 00031374001), smoothed with a gaussian with $\sigma = 7''$. The red ‘x’ marks the position of Swift J195846.1+284602.

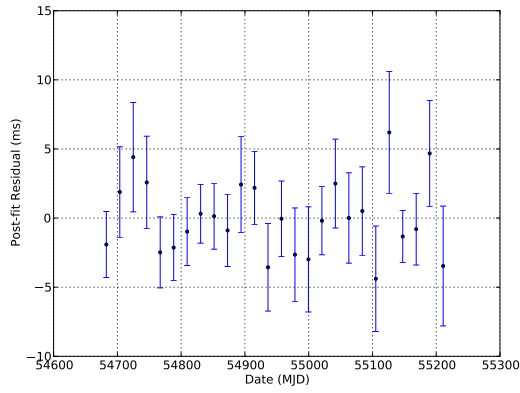


Fig. 45.— Post-fit timing residuals for PSR J1958+2846.

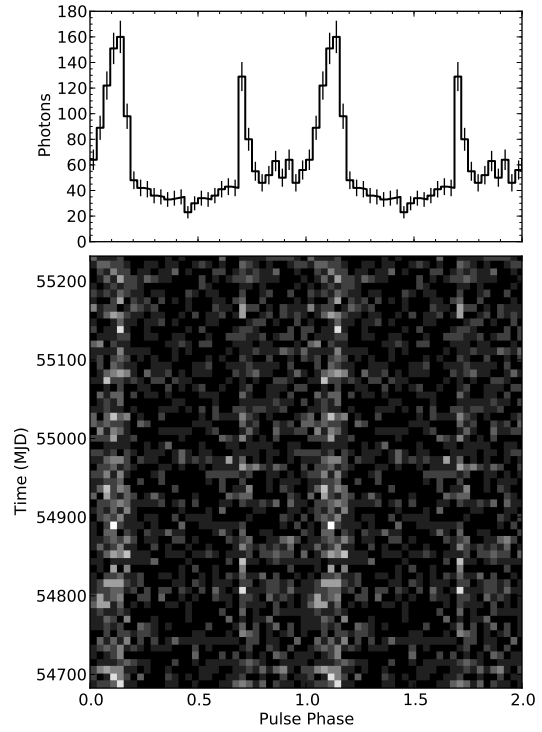


Fig. 46.— 2-D phaseogram and pulse profile of PSR J1958+2846. Two rotations are shown on the X-axis. The photons were selected according to the ROI and E_{\min} in Table 17. The fiducial point corresponding to TZRMJD is phase 0.0.

TABLE 17
PSR J1958+2846

Parameter	Value
Right ascension, α (J2000.0)	19:58:40.07 $\pm 0.03^s$
Declination, δ (J2000.0)	+28:45:54 $\pm 1''$
Monte Carlo position uncertainty	3.5''
Pulse frequency, ν (s^{-1})	3.4436537099(5)
Frequency first derivative, $\dot{\nu}$ (s^{-2}) ..	$-2.5145(2) \times 10^{-12}$
Frequency second derivative, $\ddot{\nu}$ (s^{-3})	$3(2) \times 10^{-23}$
Epoch of Frequency (MJD)	54800
TZRMJD	54957.3282188686
Number of photons (n_γ)	1910
Number of TOAs	26
RMS timing residual (ms)	2.1
Template Profile	2 Gaussian
E_{\min}	550 MeV
ROI	0.6°
Valid range	54682–55210

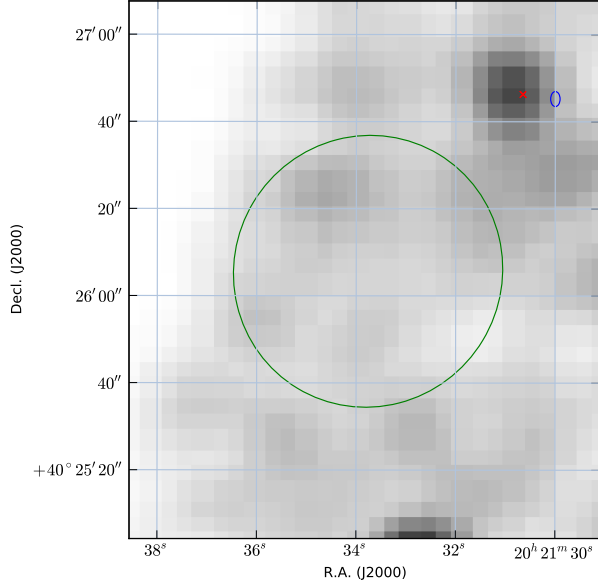


Fig. 47.— Timing position for PSR J2021+4026 (blue ellipse). The large green ellipse is the LAT position of 1FGL J2021.5+4026, based on 18 months of data. The red ‘x’ marks the position of the source S21 (see text). The background X-ray image is a portion of a *Chandra* ACIS-I image (ObsID 5533), with 3-pixel gaussian smoothing.

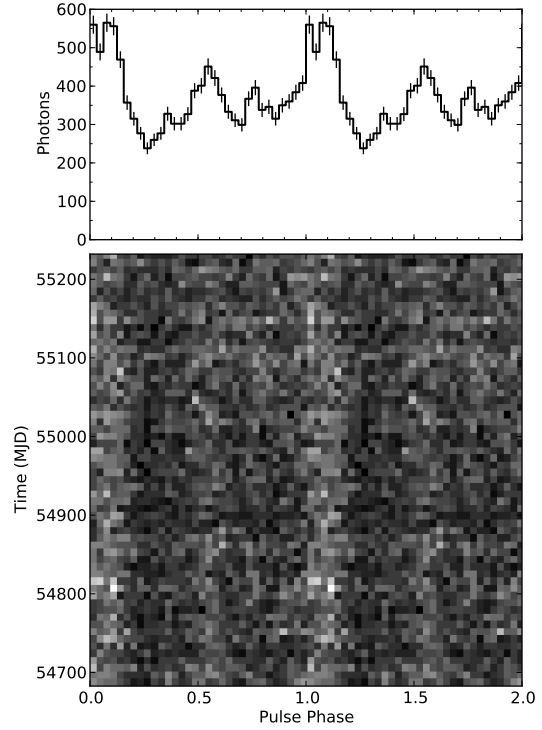


Fig. 49.— 2-D phaseogram and pulse profile of PSR J2021+4026. Two rotations are shown on the X-axis. The photons were selected according to the ROI and E_{\min} in Table 18. The fiducial point corresponding to TZRMJD is phase 0.0.

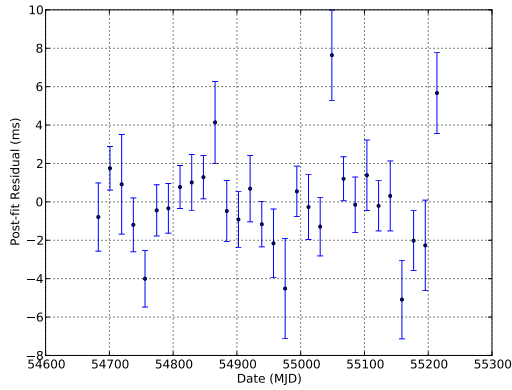


Fig. 48.— Post-fit timing residuals for PSR J2021+4026.

TABLE 18
PSR J2021+4026

Parameter	Value
Right ascension, α (J2000.0)	20:21:29.99 $\pm 0.03^s$
Declination, δ (J2000.0)	+40:26:45.1 $\pm 0.7''$
Monte Carlo position uncertainty	2.5''
Pulse frequency, ν (s^{-1})	3.7690668480(6)
Frequency first derivative, $\dot{\nu}$ (s^{-2}) ..	$-7.7681(3) \times 10^{-13}$
Frequency second derivative, $\ddot{\nu}$ (s^{-3})	$3.9(2) \times 10^{-22}$
Epoch of Frequency (MJD)	54936
TZRMJD	54957.3282196715
Number of photons (n_γ)	11853
Number of TOAs	30
RMS timing residual (ms)	2.0
Template Profile	KDE
E_{\min}	400 MeV
ROI	0.7°
Valid range	54682–55213

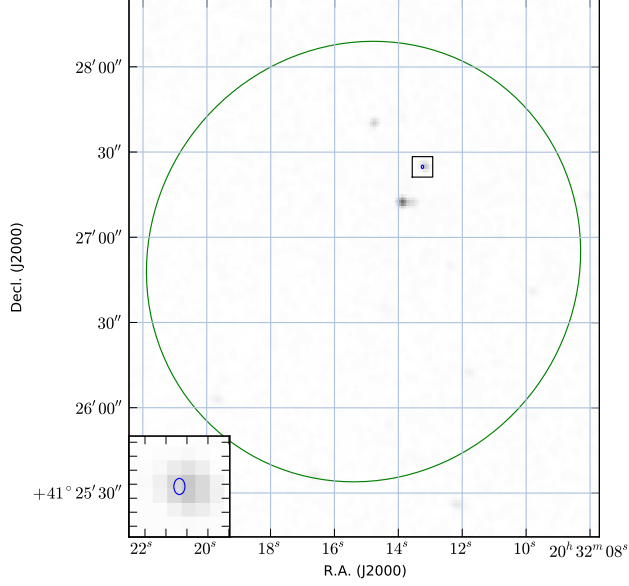


Fig. 50.— Timing position for PSR J2032+4127 (blue ellipse). The large green ellipse is the LAT position of 1FGL J2032.2+4127, based on 18 months of data. The background image is from a 49 ks Chandra ACIS observation (ObsID 4501). The inset shows a $3.6''$ region around the timing position in more detail.

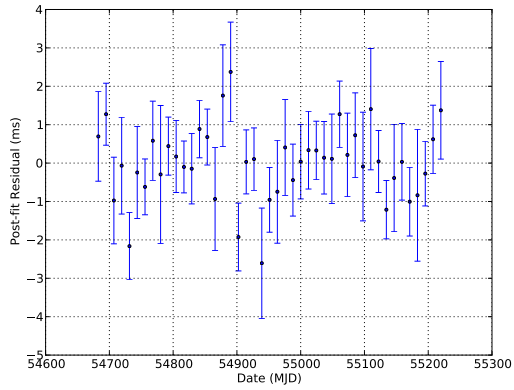


Fig. 51.— Post-fit timing residuals for PSR J2032+4127.

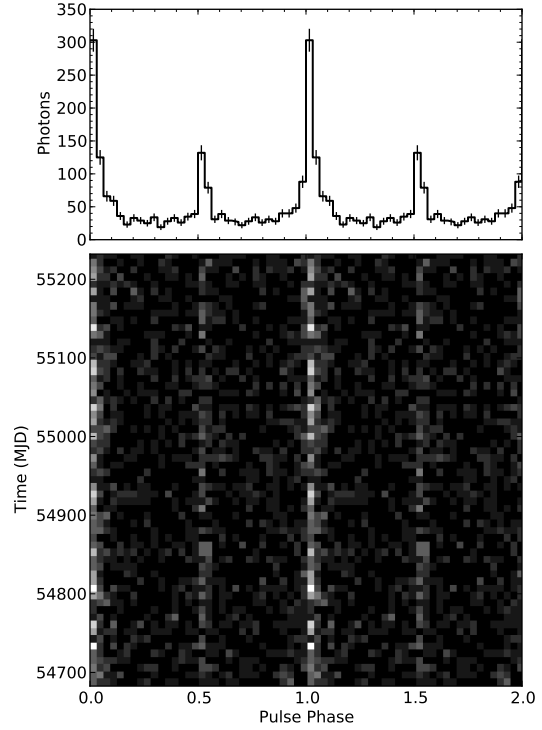


Fig. 52.— 2-D phaseogram and pulse profile of PSR J2032+4127. Two rotations are shown on the X-axis. The photons were selected according to the ROI and E_{\min} in Table 19. The fiducial point corresponding to TZRMJD is phase 0.0.

TABLE 19
PSR J2032+4127

Parameter	Value
Right ascension, α (J2000.0)	20:32:13.25 $\pm 0.01^s$
Declination, δ (J2000.0)	+41:27:24.8 $\pm 0.3''$
Monte Carlo position uncertainty	3''
Pulse frequency, ν (s^{-1})	6.9809196293(4)
Frequency first derivative, $\dot{\nu}$ (s^{-2}) ..	$-9.9293(2) \times 10^{-13}$
Frequency second derivative, $\ddot{\nu}$ (s^{-3})	$-1.88(1) \times 10^{-21}$
Epoch of Frequency (MJD)	54938
TZRMJD	54951.224402859
Number of photons (n_γ)	1633
Number of TOAs	45
RMS timing residual (ms)	0.9
Template Profile	2 Gaussian
E_{min}	900 MeV
ROI	0.5°
Valid range	54682–55220

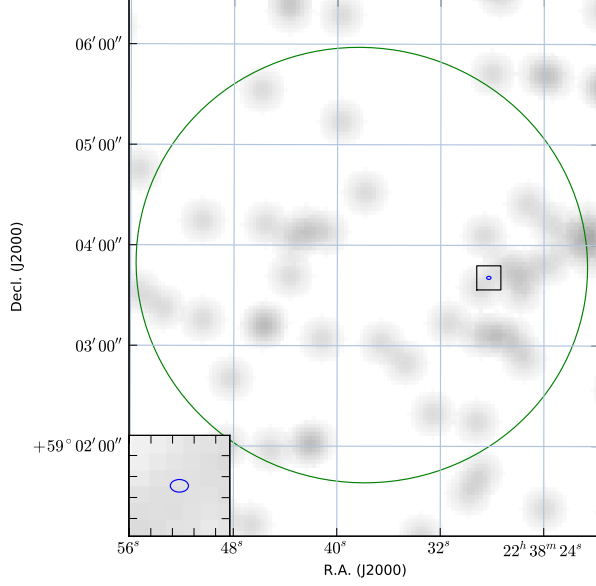


Fig. 53.— Timing position for PSR J2238+5903 (blue ellipse). The large green ellipse is the LAT position of 1FGL J2238.4+5903, based on 18 months of data. The background 0.2–10 keV X-ray image is a 4.9 ks *Swift* image (ObsID 00031398001), smoothed with a gaussian with $\sigma = 7''$. The inset shows a $7.2''$ region around the pulsar in more detail.

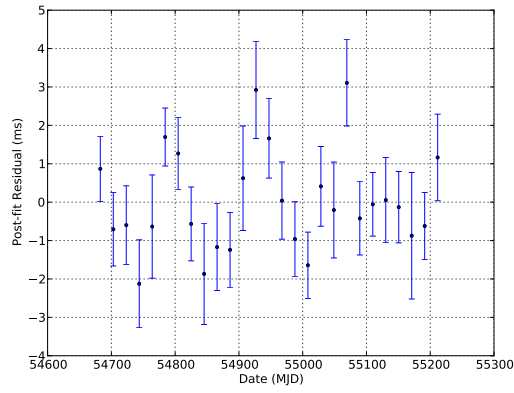


Fig. 54.— Post-fit timing residuals for PSR J2238+5903.

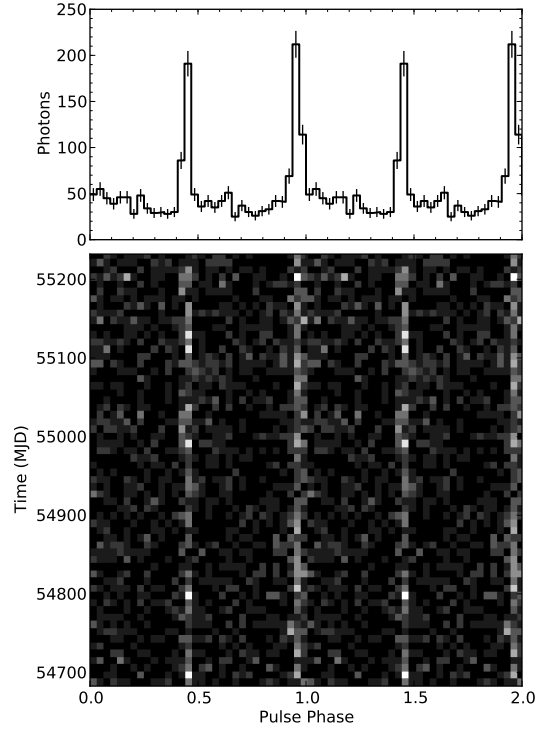


Fig. 55.— 2-D phaseogram and pulse profile of PSR J2238+5903. Two rotations are shown on the X-axis. The photons were selected according to the ROI and E_{\min} in Table 20. The fiducial point corresponding to TZRMJD is phase 0.0.

TABLE 20
PSR J2238+5903

Parameter	Value
Right ascension, α (J2000.0)	22:38:28.27 $\pm 0.04^s$
Declination, δ (J2000.0)	+59:03:40.8 $\pm 0.4''$
Monte Carlo position uncertainty	3''
Pulse frequency, ν (s^{-1})	6.1450029089(4)
Frequency first derivative, $\dot{\nu}$ (s^{-2}) ..	$-3.6641(2) \times 10^{-12}$
Frequency second derivative, $\ddot{\nu}$ (s^{-3})	$1.1(2) \times 10^{-22}$
Epoch of Frequency (MJD)	54800
TZRMJD	54947.1551907197
Number of photons (n_γ)	1697
Number of TOAs	27
RMS timing residual (μs)	1171
Template Profile	2 Gaussian
E_{\min}	250 MeV
ROI	0.5°
Valid range	54682–55211

5. Discussion

We have presented precise phase-coherent timing models using 18 months of *Fermi* LAT data for 17 radio-quiet or radio-faint γ -ray pulsars. This provides precise spin parameters for all of the pulsars and position determinations of order arcsecond accuracy.

In most cases the new position determinations served to confirm previously proposed X-ray counterparts. However, in one case (PSR J1958+2846) the previously proposed counterpart is strongly discrepant with the new position determination. In one other case (PSR J1459–6053), an X-ray source is apparent in a *Swift* image at the pulsar position. Lastly in 3 cases (PSRs J0633+0632, J1418–6058, and J2021+4026), the situation is a bit more complicated, because the observed offsets between the timing position and the X-ray counterpart position may be accounted for by the effects of timing noise on the model fits. These were covered on a case-by-case basis.

In three of the 17 pulsars (PSRs J0007+7303, J1124–5916, and J1813–1246), we have detected a glitch. This is not unexpected for a population of mostly young pulsars with characteristic ages of $10^4 - 10^5$ years. These three glitches observed in the seventeen radio quiet and radio faint pulsars are typical of the eight glitches observed in eighteen months of the *Fermi* γ -ray pulsars. All pulsars observed to glitch with the LAT pulsars have spin down energies $\dot{E} > 4.5 \times 10^{35} \text{ erg s}^{-1}$. In fact, most (6/8) of the glitching pulsars are above $\dot{E} > 1 \times 10^{36} \text{ erg s}^{-1}$. All of the LAT glitching pulsars have characteristic ages between 1–100 kyr. A more detailed analysis of timing across glitches in γ -ray pulsars is in preparation (Dormody et al. 2010, in preparation).

With 18 months of timing data, we also have measurements of $\ddot{\nu}$ for most of the pulsars. The measured $\ddot{\nu}$ s are dominated by timing noise rather than the secular spin down behavior of the pulsars. Previously, Arzoumanian et al. (1994b) have defined a pulsar stability parameter

$$\Delta(t) = \log_{10} \left(\frac{1}{6\nu} |\ddot{\nu}| t^3 \right), \quad (8)$$

where t is the observation duration and they define $\Delta_8 = \Delta(10^8 \text{s})$. They find a correlation of this stability parameter with pulsar period derivative

(\dot{P}), with the form

$$\Delta_8 = 6.6 + 0.6 \log_{10} \dot{P}. \quad (9)$$

This relationship has been re-fit using a larger sample of pulsars by Hobbs et al. (2010), who obtain the following parameters:

$$\Delta_8 = 5.1 + 0.5 \log_{10} \dot{P}. \quad (10)$$

We do not have 10^8 s of data, so we compute our Δ parameter at $t = 10^{7.6} \text{ s}$. As seen in Figure 56, we see a similar correlation with period derivative, albeit with a large amount of scatter. The two pulsars that stand out farthest from the relation as having very large $\ddot{\nu}$ for their period derivatives are PSRs J2021+4026 and J2032+4127.

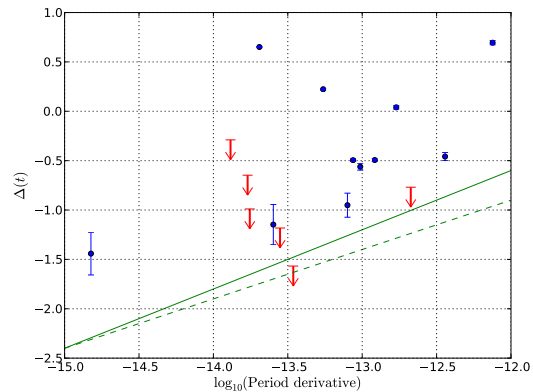


Fig. 56.— Δ parameter characterizing timing noise vs. $\dot{\nu}$ for these pulsars. The red arrows represent $2\text{-}\sigma$ upper limits. The solid green line is the relation for Δ_8 found by Arzoumanian et al. (1994b), while the dashed line is the relation found by Hobbs et al. (2010). Note that our data span is about half of the 10^8 s used in the definition of Δ_8 .

These pulsars will continue to be timed regularly throughout the LAT mission. Using the fake TOA simulation capability of TEMPO2, we have evaluated the possibility of measuring further astrometric parameters for these pulsars. We find that in a 10 year mission, we are unlikely to be able to detect parallax or proper motion for any of these sources. The most nearby pulsar is $\sim 400 \text{ pc}$ distant, and a parallax signal at that distance is $3 \mu\text{s}$, for a pulsar at an ecliptic latitude of 0. Unfortunately, the nearby pulsars are also those with

the longest periods and the largest RMS timing residuals. We evaluated the possibility of detecting proper motion for a large transverse velocity of 1000 km s^{-1} , and again found that none of the pulsars look like promising candidates for proper motion measurements within the *Fermi* mission.

We also made deep searches for radio pulsations from the γ -ray selected pulsars. We compare these flux limits with the measured fluxes of the population of pulsars in the ATNF pulsar catalog (Manchester et al. 2005) in Figure 57. To make the fluxes comparable, we have scaled them all to the equivalent 1400 MHz flux density using a typical pulsar spectral index of 1.6. The upper limits we have obtained are comparable to some of the faintest known radio pulsars, but the discovery of $3.5 \mu\text{Jy}$ pulsations from PSR J1907+0602 (Abdo et al. 2010c) raises the possibility that some of these could yet be detected in even deeper radio searches.

The radio upper limits for 8 new γ -ray selected pulsar discovered with *Fermi* are presented in Saz Parkinson et al. (2010). When combined with the results presented here, we now have deep upper limits on all known γ -ray selected pulsars. A discussion of the radio upper limits on PSR J1836+5925 was also presented by Abdo et al. (2010a).

The authors gratefully acknowledge Masaharu Hirayama and the rest of the developers of the LAT Science Tools used for pulsar timing. This work makes use of APLpy by Eli Bressert and Thomas Robitaille.

The *Fermi* LAT Collaboration acknowledges generous ongoing support from a number of agencies and institutes that have supported both the development and the operation of the LAT as well as scientific data analysis. These include the National Aeronautics and Space Administration and the Department of Energy in the United States, the Commissariat à l’Energie Atomique and the Centre National de la Recherche Scientifique / Institut National de Physique Nucléaire et de Physique des Particules in France, the Agenzia Spaziale Italiana and the Istituto Nazionale di Fisica Nucleare in Italy, the Ministry of Education, Culture, Sports, Science and Technology (MEXT), High Energy Accelerator Research Organization (KEK) and Japan Aerospace Exploration Agency

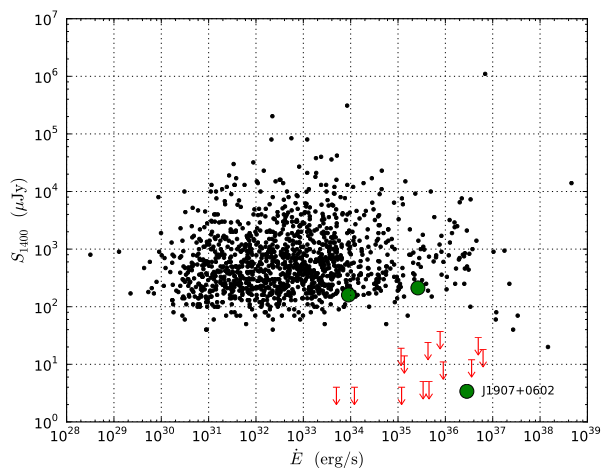


Fig. 57.— Summary of radio pulsation searches of γ -ray selected pulsars. The red arrows denote upper limits for the non-detections reported in Table 3. The large green dots are the radio pulsation detections that have been previously reported (Camilo et al. 2009; Abdo et al. 2010c). The black dots are the 1400 MHz flux densities of the non-millisecond pulsars in the ATNF catalog, for comparison. The detections and upper limits that were made at different observing frequencies were scaled to 1400 MHz using a typical pulsar spectral index of 1.6.

(JAXA) in Japan, and the K. A. Wallenberg Foundation, the Swedish Research Council and the Swedish National Space Board in Sweden.

Additional support for science analysis during the operations phase is gratefully acknowledged from the Istituto Nazionale di Astrofisica in Italy and the Centre National d'Études Spatiales in France.

The Arecibo Observatory is part of the National Astronomy and Ionosphere Center, which is operated by Cornell University under a cooperative agreement with the National Science Foundation. The National Radio Astronomy Observatory is a facility of the National Science Foundation operated under cooperative agreement by Associated Universities, Inc. The Parkes Observatory is part of the Australia Telescope which is funded by the Commonwealth of Australia for operation as a National Facility managed by CSIRO.

Facilities: Fermi LAT, GBT, Arecibo, Parkes

REFERENCES

- Abdo, A. A., et al. 2008, *Science*, 322, 1218, (CTA1)
- . 2009a, *Science*, 325, 840, (16 Blind Search Pulsars)
- . 2009b, *ApJS*, 183, 46, (LAT Bright Source List)
- . 2009c, *Science*, 326, 1512, (Cyg X-3)
- . 2010a, *ApJ*, 712, 1209, (PSR J1836+5925)
- . 2010b, *ApJ*, 720, 272, (Geminga)
- . 2010c, *ApJ*, 711, 64, (PSR J1907+0602)
- . 2010d, *ApJS*, 187, 460, (LAT Pulsar Catalog)
- . 2010e, *ApJ*, 713, 154, (Vela2)
- . 2011, *ApJS*, in press (Erratum to *ApJS*, 187, 460)
- Andersson, N., Comer, G. L., & Prix, R. 2003, *Physical Review Letters*, 90, 091101
- Arzoumanian, Z., Nice, D. J., Taylor, J. H., & Thorsett, S. E. 1994a, *ApJ*, 422, 671
- . 1994b, *ApJ*, 422, 671
- Atwood, W. B., et al. 2009, *ApJ*, 697, 1071
- Becker, W., et al. 2004, *ApJ*, 615, 897
- Braje, T. M., Romani, R. W., Roberts, M. S. E., & Kawai, N. 2002, *ApJ*, 565, L91
- Camilo, F., Manchester, R. N., Gaensler, B. M., Lorimer, D. R., & Sarkissian, J. 2002, *ApJ*, 567, L71
- Camilo, F., et al. 2009, *ApJ*, 705, 1
- Cordes, J. M., & Downs, G. S. 1985, *ApJS*, 59, 343
- Cordes, J. M., & Lazio, T. J. W. 2002, *arXiv:astro-ph/0207156*
- de Jager, O. C., Raubenheimer, B. C., & Swanepoel, J. W. H. 1986, *A&A*, 170, 187
- . 1989, *A&A*, 221, 180
- Edwards, R. T., Hobbs, G. B., & Manchester, R. N. 2006, *MNRAS*, 372, 1549
- Faucher-Giguère, C., & Kaspi, V. M. 2006, *ApJ*, 643, 332
- Gonthier, P. L., Story, S. A., Clow, B. D., & Harding, A. K. 2007, *Ap&SS*, 309, 245
- Halpern, J. P., Camilo, F., & Gotthelf, E. V. 2007, *ApJ*, 668, 1154
- Halpern, J. P., Gotthelf, E. V., Camilo, F., Helfand, D. J., & Ransom, S. M. 2004, *ApJ*, 612, 398
- Hobbs, G., Lyne, A. G., & Kramer, M. 2010, *MNRAS*, 402, 1027
- Hobbs, G., Lyne, A. G., Kramer, M., Martin, C. E., & Jordan, C. 2004, *MNRAS*, 353, 1311
- Hobbs, G. B., Edwards, R. T., & Manchester, R. N. 2006, *MNRAS*, 369, 655
- Jackson, M. S., & Halpern, J. P. 2005, *ApJ*, 633, 1114
- Kramer, M., & Wex, N. 2009, *Classical and Quantum Gravity*, 26, 073001
- Link, B., Epstein, R. I., & Lattimer, J. M. 1999, *Physical Review Letters*, 83, 3362
- Livingstone, M. A., Ransom, S., Camilo, F., Kaspi, V. M., Lyne, A., Kramer, M., & Stairs, I. H. 2009, *ApJ*, 706, 1163, submitted (arXiv:0901.2119)
- Lorimer, D., & Kramer, M. 2005, *Handbook of Pulsar Astronomy* (Cambridge University Press)
- Manchester, R. N., Hobbs, G. B., Teoh, A., & Hobbs, M. 2005, *AJ*, 129, 1993
- Ng, C., Roberts, M. S. E., & Romani, R. W. 2005, *ApJ*, 627, 904
- Ransom, S. M., Eikenberry, S. S., & Middleditch, J. 2002, *AJ*, 124, 1788
- Roberts, M. 2009, talk presented at Supernova Remnants And Pulsar Wind Nebulae In The Chandra Era, July 2009, <http://cxc.harvard.edu/cdo/snr09/program.html>

- Roberts, M. S. E. 2008, in American Institute of Physics Conference Series, Vol. 983, 40 Years of Pulsars: Millisecond Pulsars, Magnetars and More, ed. C. Bassa, Z. Wang, A. Cumming, & V. M. Kaspi, 621–623
- Roberts, M. S. E., Hessels, J. W. T., Ransom, S. M., Kaspi, V. M., Freire, P. C. C., Crawford, F., & Lorimer, D. R. 2002, *ApJ*, 577, L19
- Roberts, M. S. E., Romani, R. W., & Kawai, N. 2001, *ApJS*, 133, 451
- Saz Parkinson, P. M., et al. 2010, *ApJ*, 725, 571
- Seidelmann, P. K. 1992, Explanatory Supplement to the Astronomical Almanac (University Science Books)
- Smith, D. A., et al. 2008, *A&A*, 492, 923
- Stairs, I. H. 2003, *Living Reviews in Relativity*, 6, 5
- Standish, E. M. 1998, JPL IOM 312.F-98-048
- Story, S. A., Gonthier, P. L., & Harding, A. K. 2007, *ApJ*, 671, 713
- Taylor, J. H. 1992, Royal Society of London Philosophical Transactions Series A, 341, 117
- Taylor, J. H., Fowler, L. A., & McCulloch, P. M. 1979, *Nature*, 277, 437
- Theureau, G., Parent, D., Cognard, I., et al. 2010, *A&A*, in press
- Trepl, L., Hui, C. Y., Cheng, K. S., Takata, J., Wang, Y., Liu, Z. Y., & Wang, N. 2010, *MNRAS*, 405, 1339
- Watters, K. P., Romani, R. W., Weltevrede, P., & Johnston, S. 2009, *ApJ*, 695, 1289
- Weisskopf, M. C., et al. 2006, *ApJ*, 652, 387
- Yadigaroglu, I., & Romani, R. W. 1995, *ApJ*, 449, 211
- Zavlin, V. E., Pavlov, G. G., & Shibano, Y. A. 1996, *A&A*, 315, 141

A. Calculation of Position Offsets

The light travel time delay τ (i.e. Roemer delay) across the solar system from a pulsar at ecliptic coordinates λ (longitude) and β (latitude) is:

$$\tau \simeq 500 \text{ s } \cos(\beta) \cos(\theta(t) + \lambda), \quad (\text{A1})$$

where $\theta(t)$ is the orbital phase of the Earth with respect to the vernal equinox. This is an approximate time delay since we are assuming that the Earth's orbit is circular.

If a pulsar is being timed with incorrect ecliptic coordinates such that there exist position offsets $\Delta\lambda$ and $\Delta\beta$, there will be a differential time delay $\Delta\tau$ present in the timing residuals:

$$\Delta\tau \simeq 500 \text{ s } [\cos(\beta + \Delta\beta) \cos(\theta(t) + \lambda + \Delta\lambda) - \cos(\beta) \cos(\theta(t) + \lambda)]. \quad (\text{A2})$$

If the positional offsets are small, such that we can use $\sin x \sim x$, $\cos x \sim 1$, and $\Delta\beta \Delta\lambda \sim 0$, we can use trigonometric identities to get:

$$\Delta\tau \simeq -500 \text{ s } [\Delta\lambda \cos(\beta) \sin(\theta(t) + \lambda) + \Delta\beta \sin(\beta) \cos(\theta(t) + \lambda)]. \quad (\text{A3})$$

Comparing the trigonometric identity $A \sin(\theta(t) + \phi) = A \cos \phi \sin \theta(t) + A \sin \phi \cos \theta(t)$ to the equation for $\Delta\tau$, we see that:

$$A \cos \phi = -500 \text{ s } \Delta\lambda \cos \beta \quad (\text{A4})$$

$$A \sin \phi = -500 \text{ s } \Delta\beta \sin \beta, \quad (\text{A5})$$

and therefore:

$$\Delta\lambda = -\frac{A \cos \phi}{500 \text{ s } \cos \beta} \quad (\text{A6})$$

$$\Delta\beta = -\frac{A \sin \phi}{500 \text{ s } \sin \beta}, \quad (\text{A7})$$

The sinusoid amplitude A and phase ϕ come from fits to TOA residuals. One way of doing this is by adding a binary model to a TEMPO2 fit with parameters A1 ($A=A1$) and T0 (with PB=365.2424, the solar year; OM=0; and E=0 all held fixed in the fit). Then,

$$\phi = 2\pi \frac{\text{fmod}(\text{T0} - 51623.31250, 365.2424)}{365.2424} + \lambda + \alpha. \quad (\text{A8})$$

where `fmod` is the floating point remainder function, 51623.31250 is the MJD of the vernal equinox in 2000 and α is a correction for Earth's non-circular orbit that can be measured for a particular point in the sky by fitting for T0 at several values of simulated position offset in the ecliptic longitude direction only. In that case, $\Delta\beta = 0$, and $\phi = 0$, allowing us to solve for α .